

# Micromagnetic Tomography for Paleomagnetism and Rock-Magnetism

Lennart de Groot<sup>1</sup>, Karl Fabian<sup>2</sup>, Annemarieke Béguin<sup>2</sup>, Martha Kusters<sup>1</sup>, David Cortés-Ortuño<sup>1</sup>, Roger Fu<sup>3</sup>, Chloë Jansen<sup>1</sup>, Richard Harrison<sup>4</sup>, Tristan van Leeuwen<sup>5</sup>, and Auke Barnhoorn<sup>6</sup>

<sup>1</sup>Utrecht University

<sup>2</sup>Norwegian University of Science and Technology

<sup>3</sup>Harvard University

<sup>4</sup>University of Cambridge

<sup>5</sup>Centrum Wiskunde en Informatica, Universiteit Utrecht

<sup>6</sup>Delft University of Technology

November 23, 2022

## Abstract

Our understanding of the past behavior of the geomagnetic field arises from magnetic signals stored in geological materials, e.g. (volcanic) rocks. Bulk rock samples, however, often contain magnetic grains that differ in chemistry, size and shape; some of them record the Earth's magnetic field well, others are unreliable. The presence of a small amount of adverse behaved magnetic grains in a sample may already obscure important information on the past state of the geomagnetic field. Recently it was shown that it is possible to determine magnetizations of individual grains in a sample by combining X-ray computed tomography and magnetic surface scanning measurements. Here we establish this new Micromagnetic Tomography (MMT) technique and make it suitable for use with different magnetic scanning techniques, and for both synthetic and natural samples. We acquired reliable magnetic directions by selecting subsets of grains in a synthetic sample, and we obtained rock-magnetic information of individual grains in a volcanic sample. This illustrates that MMT opens up entirely new venues of paleomagnetic and rock-magnetic research. MMT's unique ability to determine the magnetization of individual grains in a nondestructive way allows for a systematic analysis of how geological materials record and retain information on the past state of the Earth's magnetic field. Moreover, by interpreting only the contributions of known magnetically well-behaved grains in a sample MMT has the potential to unlock paleomagnetic information from even the most complex, crucial, or valuable recorders that current methods are unable to recover.

# Micromagnetic Tomography for Paleomagnetism and Rock-Magnetism

Lennart V. de Groot<sup>1</sup>, Karl Fabian<sup>2</sup>, Annemarieke Béguin<sup>1,2</sup>, Martha E. Kusters<sup>1</sup>, David Cortés-Ortuño<sup>1</sup>, Roger R. Fu<sup>3</sup>, Chloë M.L. Jansen<sup>1</sup>, Richard J. Harrison<sup>4</sup>, Tristan van Leeuwen<sup>5,6</sup>, Auke Barnhoorn<sup>7</sup>

<sup>1</sup>Paleomagnetic laboratory Fort Hoofddijk, Faculty of Geosciences, Utrecht University, Utrecht, The Netherlands

<sup>2</sup>Department of Geoscience and Petroleum, Norwegian University of Science and Technology, Trondheim, Norway

<sup>3</sup>Department of Earth and Planetary Sciences, Harvard University, Cambridge, MA, USA

<sup>4</sup>Department of Earth Sciences, University of Cambridge, Cambridge, UK

<sup>5</sup>Mathematical Institute, Faculty of Sciences, Utrecht University, Utrecht, The Netherlands

<sup>6</sup>Department of Computational Imaging, Centrum Wiskunde & Informatica (CWI), The Netherlands

<sup>7</sup>Department of Geoscience and Engineering, Faculty of Civil Engineering and Geosciences, Delft University of Technology, Delft, The Netherlands

## Key Points:

- Micromagnetic Tomography enables determining, selecting, and interpreting magnetizations of individual grains in a sample
- We obtained magnetic directions and rock-magnetic information from subsets of grains in both a synthetic and a natural sample
- Micromagnetic Tomography has the potential to unlock magnetic information from even the most complex recorders that currently goes obscured

---

Corresponding author: Lennart V. de Groot, [l.v.degroot@uu.nl](mailto:l.v.degroot@uu.nl)

**Abstract**

Our understanding of the past behavior of the geomagnetic field arises from magnetic signals stored in geological materials, e.g. (volcanic) rocks. Bulk rock samples, however, often contain magnetic grains that differ in chemistry, size and shape; some of them record the Earth's magnetic field well, others are unreliable. The presence of a small amount of adverse behaved magnetic grains in a sample may already obscure important information on the past state of the geomagnetic field. Recently it was shown that it is possible to determine magnetizations of individual grains in a sample by combining X-ray computed tomography and magnetic surface scanning measurements. Here we establish this new Micromagnetic Tomography (MMT) technique and make it suitable for use with different magnetic scanning techniques, and for both synthetic and natural samples. We acquired reliable magnetic directions by selecting subsets of grains in a synthetic sample, and we obtained rock-magnetic information of individual grains in a volcanic sample. This illustrates that MMT opens up entirely new venues of paleomagnetic and rock-magnetic research. MMT's unique ability to determine the magnetization of individual grains in a nondestructive way allows for a systematic analysis of how geological materials record and retain information on the past state of the Earth's magnetic field. Moreover, by interpreting only the contributions of known magnetically well-behaved grains in a sample MMT has the potential to unlock paleomagnetic information from even the most complex, crucial, or valuable recorders that current methods are unable to recover.

**Plain Language Summary**

Our understanding of the past behavior of the Earth's magnetic field relies on our ability to interpret magnetic signals from rocks. Currently, we measure bulk samples consisting of many magnetic grains at once. Not all magnetic grains are good recorders of the geomagnetic field. The presence of even small amounts of adverse behaved grains in a sample already obscures vital information about the Earth's magnetic field. Here we present and establish a new method that determines magnetizations of individual grains in a sample: Micromagnetic Tomography. This new and exciting method allows to select and interpret only magnetizations of grains that are known good recorders in a sample. This will unlock magnetic information from even the most complex, crucial, or valuable samples that current methods are unable to recover.

## 54 **1 Introduction**

55 To understand the behavior of the Earth’s magnetic field, and possibly even pre-  
56 dict its future behavior, it is paramount to understand its past. Our understanding of  
57 the behavior of the geomagnetic field arises from magnetic signals stored in geological  
58 and archeological materials. They acquire a magnetization when they cool in the Earth’s  
59 magnetic field, and retain that magnetization over (geological) timescales. Igneous rocks,  
60 e.g. lavas, are the only recorders of the direction and the intensity of the field that are  
61 available throughout geologic history and all over the globe. Since lavas take snapshots  
62 of the state of the Earth’s magnetic field for their location and point in time when they  
63 cool, frequently erupting volcanic regions with well-dated volcanic products are inval-  
64 uable archives of past variations in the Earth’s magnetic field (e.g.: de Groot et al., 2013;  
65 Cromwell et al., 2015; Greve et al., 2017).

66 When a volcano erupts and lava cools on its flanks the lava solidifies to form ex-  
67 trusive igneous rocks, often of basaltic composition. A small, but significant, portion of  
68 the minerals that together constitute these basalts has magnetic properties. Lavas are  
69 often regarded to be excellent paleomagnetic recorders, but over the past years evidence  
70 piled up that their magnetic signal is often compromised. This has been known for a long  
71 time for reconstructions of variations in field strength. Viscous changes in the magnetic  
72 signal of natural rocks (e.g.: Shaar et al., 2011; de Groot, Fabian, et al., 2014) or ther-  
73 mochemical changes during laboratory experiments (e.g.: Fabian, 2009; Shcherbakov et  
74 al., 2019) frequently hamper paleointensity experiments (Tauxe & Yamazaki, 2015). But  
75 even obtaining a paleomagnetic direction from volcanic samples is not always straight-  
76 forward, as illustrated by a recent reappraisal of the paleomagnetic signal stored in a stack  
77 of lava flows from Steens Mountain (Coe et al., 2014), that falsified a previous interpre-  
78 tation of a very rapid change in the direction of the Earth’s magnetic field during a ge-  
79 omagnetic polarity reversal (Prévot et al., 1985).

80 Almost all experiments to determine the past state of the Earth’s magnetic field  
81 from rocks use bulk samples (usually  $\sim 10$  cc) and measure their magnetic moment af-  
82 ter series of laboratory treatments. Lavas consist of mixtures of different iron-oxides that  
83 vary in size, shape, and chemistry. These iron-oxide grains are the actual magnetic recorders  
84 in the samples. Some of these grains record the Earth’s magnetic field well; others may  
85 not able to provide reliable information on its past state. When measuring a typical pa-

86 leomagnetic sample, the magnetic moments of millions of grains are measured simulta-  
87 neously and result in one magnetic moment for the entire sample. A small amount of  
88 adverse behaved magnetic grains in a sample already hampers any classical experiment  
89 to obtain paleointensities. Therefore, these experiments often fail and success rates as  
90 low as 10-20% are common (Valet, 2003; Tauxe & Yamazaki, 2015). This implies that  
91 for 80-90% of all lavas vital information on paleointensities is lost before it can be un-  
92 covered.

93 The iron-oxide grains in a lava acquire a magnetization that is proportional to the  
94 ambient magnetic field during cooling; such magnetizations are referred to as ‘thermore-  
95 manent magnetizations’ (TRMs). The magnetic properties of iron-oxide grains vary dra-  
96 matically due to differences in grain size, shape, chemistry and thermal history as sum-  
97 marized by Dunlop and Özdemir (1997). The magnetic behavior of very small ‘single do-  
98 main’ iron-oxides (30-60 nm) is described by Néel’s theory on thermoremanent magne-  
99 tizations in single-domain ferromagnetic minerals (Néel, 1949, 1955). These grains are  
100 magnetically well-behaved; if a sample would consist of only such small grains it would  
101 be relatively straightforward to obtain a reliable estimate of both the paleodirection and  
102 paleointensity of the Earth’s magnetic field using classical paleomagnetic techniques. Un-  
103 fortunately, iron-oxides in naturally occurring lavas are generally much larger (up to >50  
104  $\mu\text{m}$ ). Not only do these ‘multi-domain’ grains violate Néel’s theory, they also often vi-  
105 olate Thellier’s laws of reciprocity, independence and additivity (e.g.: Thellier & Thel-  
106 lier, 1959; Coe, 1967; Shcherbakova et al., 2000; Fabian, 2000, 2001; Dunlop, 2011; Tauxe  
107 & Yamazaki, 2015). Moreover, these multi-domain grains may be prone to unstable mag-  
108 netizations over time caused by e.g. viscous reordering of magnetic domains (de Groot,  
109 Fabian, et al., 2014), or time and temperature dependent cation reordering (Bowles et  
110 al., 2013; Bowles & Jackson, 2016). In contrast to Néel’s theory for single domain grains,  
111 there currently is no comprehensive, fundamental theory for the processes governing the  
112 acquisition and preservation of magnetic signals in multi-domain grains; i.e. their mag-  
113 netic behavior still is enigmatic – although they make up the vast majority of the rema-  
114 nence carrying grains in igneous rocks.

115 If we would be able to determine the magnetic moments of individual mineral grains  
116 inside a natural sample in a non-destructive way, we could determine which naturally  
117 occurring iron-oxide grains record the Earth’s magnetic field well, and which are unre-  
118 liable. This would enable us to select and consider only the magnetic contributions of

119 known well-behaved magnetic grains, and reject the contributions of others. Thereby we  
120 could fully unlock the paleomagnetic information stored in all sorts of geological mate-  
121 rials, even if large amounts of adverse behaved magnetic minerals are present in the sam-  
122 ple. This will provide indispensable data to understand the behavior of the geomagnetic  
123 field on decadal to centennial time scales, and possibly enables predictions of its future  
124 behavior.

125 Information about the magnetic state of individual grains in a sample can theo-  
126 retically be obtained from scans of magnetic anomalies on the surface of a sample, if the  
127 spatial resolution permits. The rock-magnetic interpretation of these magnetic surface  
128 scans, however, is notoriously difficult. The classical potential inversion problem (Kellogg,  
129 1929) states that it is impossible to obtain unique information on the distribution of mag-  
130 netic sources (i.e. our grains) within a body (i.e. our sample), based on observations of  
131 the magnetization outside this body alone. Additional information or assumptions are  
132 necessary to characterize the magnetic sources (Lima & Weiss, 2009; Lima et al., 2013).  
133 Currently, the interpretation of these magnetic maps is often done by an ‘upward con-  
134 tinuation’ of the magnetic measurements: the magnetic signal for the entire sample or  
135 region is inferred by calculating the resulting magnetic moment further away from the  
136 sample (Blakely, 1996; Lima & Weiss, 2009; Lima et al., 2014; Lima & Weiss, 2016; Fu  
137 et al., 2020). This implicitly averages the magnetic contributions present in the region  
138 of interest, without the possibility to assess or consider the quality of individual grains  
139 as paleomagnetic recorders.

140 We recently overcame the non-uniqueness of the classical potential inversion prob-  
141 lem by adding the results of an X-ray Computed Tomography (microCT) scan to the re-  
142 sults of scanning magnetometry (de Groot et al., 2018). The microCT scan determines  
143 the exact locations, sizes and shapes of the iron-oxides grains in a sample, which ensures  
144 that our inversion routine can now only attribute magnetizations from the surface mag-  
145 netometry to the magnetic grains in our sample. The additional microCT information  
146 therefore enables a unique inversion of the information produced by scanning magnetom-  
147 etry without the necessity of any further assumptions (Fabian & de Groot, 2019). With  
148 this newly developed technique now known as Micro-Magnetic Tomography (MMT) the  
149 individual magnetic moments of 20 grains inside a synthetic sample were successfully de-  
150 termined (de Groot et al., 2018). The synthetic sample used in this study, however, was  
151 optimized for success: its concentration of magnetic grains was one to two orders of mag-

152 nitude lower compared to natural samples; and pure magnetite grains with a well-defined  
153 suite of grain sizes were used - in contrast to the large variation in grain sizes and chem-  
154 istry of naturally occurring iron-oxides. Given these characteristics of the synthetic sam-  
155 ple and the amount of grains for which magnetic moments were determined, the MMT  
156 study by de Groot et al. (2018) is fore-mostly a proof-of-concept. Here we build on this  
157 proof-of-concept and (1) show that the MMT technique is universally applicable by us-  
158 ing different magnetic scanning techniques, (2) up-scale the technique to be useful for  
159 natural (volcanic) samples; (3) show that it is possible to acquire magnetic directions  
160 by selecting subsets of grains present in a sample using MMT; and (4) acquire a rock-  
161 magnetic characterization of grains in a volcanic sample from MMT. This firmly estab-  
162 lishes MMT as a new paleomagnetic and rock-magnetic technique that is useful to un-  
163 lock information from samples with complex magnetic behavior that current paleomag-  
164 netic and rock-magnetic methods are unable to recover.

## 165 **2 Micromagnetic Tomography**

166 The MMT technique determines the magnetic moments of individual grains in a  
167 sample by inverting a two-dimensional magnetic surface scan of the sample based on the  
168 known locations and shapes of the iron-oxide grains as determined by a microCT scan  
169 of the sample. The input for any MMT experiment is thus (1) a magnetic surface scan,  
170 and (2) a microCT characterization of the sample (Fig. 1). These two data sets must  
171 first be co-registered into a common spatial coordinate system, before a mathematical  
172 inversion of the magnetic surface scan constrained by the microCT data can produce the  
173 magnetic moments of the grains. The accuracy of the inversion results can then be as-  
174 sessed by determining the residuals left by the inversion.

### 175 **2.1 MicroCT analysis**

176 The locations, sizes, and shapes of the iron-oxide grains in a sample are determined  
177 using a microCT scan. This technique produces a three-dimensional image of the X-ray  
178 attenuation contrast in a sample, that is often interpreted in terms of variations in den-  
179 sity in the sample (Sakellariou et al., 2004; Madonna et al., 2012; Jussiani & Appoloni,  
180 2015). The densities of iron-oxides (e.g. magnetite: 5.2, hematite: 5.3,  $\text{ilvospinel}$ : 4.8,  
181 and  $\text{ilmenite}$ :  $4.8 \times 10^3 \text{ kg/m}^3$ ) are generally 1.4 to 2 times larger than the densities of  
182 other common minerals in basalt (e.g. plagioclases: 2.6–2.8, and pyroxenes 3.2–3.9

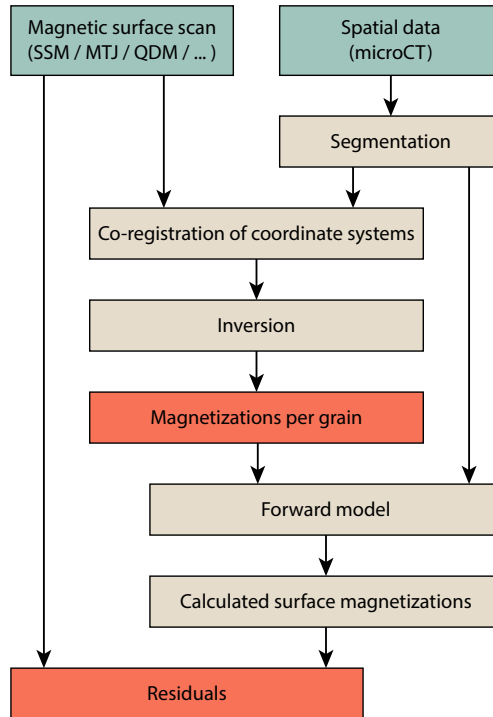


**Figure 1.** Workflow of Micromagnetic Tomography experiments. The input (measurements) is in the green boxes; computational steps are in the tan boxes; and the output is in the red boxes.

183  $10^3 \text{ kg/m}^3$ ), although the heavier olivines ( $3.2\text{--}4.4 \times 10^3 \text{ kg/m}^3$ ), have a less profound  
 184 difference (density data from [www.mindat.org](http://www.mindat.org)). Because of these large density differ-  
 185 ences between iron-oxide minerals and other minerals and/or (synthetic) matrices present  
 186 in a sample, the attenuation contrast in microCT scans generally allows to precisely lo-  
 187 cate all iron-oxides with volumes above the voxel limit, and also to estimate their shape  
 188 and volume within the limits of the voxel representation.

189 When using microCT data it is up to the interpreter to make selections in the at-  
 190 tenuation contrast spectrum in the sample for the segmentation of individual iron-oxide  
 191 grains by setting a density threshold above which voxels are deemed to belong to iron  
 192 oxide grains. The well-defined differences in density between the iron-oxides and the other  
 193 common minerals in basalt typically yield a bi-modal or multi-modal attenuation spec-  
 194 trum in the microCT analysis, and the minimum separating the high-density peaks from  
 195 the lower density matrix minerals can be selected as threshold. It is important to set the  
 196 threshold such that all iron-oxide grains are included in the analysis, even if this implies  
 197 that some non-magnetic grains are also selected. After all, a grain that is selected can

198 be assigned a (near) zero magnetization by the inversion, but missing an iron-oxide grain  
199 in the microCT analysis leads to magnetic anomalies in the magnetic surface scan that  
200 cannot be properly assigned to their source. Setting the threshold for the attenuation  
201 contrast results in a list of voxels with their spatial coordinates that pass this selection.  
202 Groups of adjacent, interconnected, high-density voxels form a precisely localized grain,  
203 for which also the size and shape are now approximately known. From these data the  
204 volume, center of gravity, and distance to e.g. the surface of the sample can be estimated  
205 for each grain individually.

206 The volume uncertainty related to voxel thresholding is difficult to assess because  
207 it critically depends on the grain's shape. The fact that a thin iron-oxide plate with large  
208 volume but thickness below a fraction of the voxel width  $\epsilon$  would not be recognized shows  
209 that the error can be arbitrarily large. For bodies with surface area  $A$  and volume  $V$  the  
210 relative volume uncertainty is in the order of  $A\epsilon/V$ , and thus for sphere-like bodies with  
211 diameter  $D$  decreases with  $\epsilon/D$ . For the MMT technique the most important informa-  
212 tion is the location and topological separation of the iron-oxide grain or cluster which  
213 will be assigned a separate magnetic moment by the inversion. Only the interpretation  
214 of this magnetic moment in terms of a grain's magnetization requires the grain's volume  
215 with its much larger uncertainty due to voxel binarization (Heidig et al., 2017).

## 216 **2.2 Scanning magnetometry**

217 Recent advances in scanning magnetometry techniques such as Scanning SQUID  
218 Magnetometry (SSM) (Egli & Heller, 2000; Weiss et al., 2007; Lima & Weiss, 2016), in-  
219 struments using a Magnetic Tunnel Junction (MTJ) (Lima et al., 2014), and the Quan-  
220 tum Diamond Microscope (QDM) (Glenn et al., 2017; Farchi et al., 2017; Levine et al.,  
221 2019; Fu et al., 2020) allow for quantitative measurements of the magnetic field on, or  
222 near, the surface of a sample in (sub)micrometer resolution. In theory, results from all  
223 these magnetic surface magnetometry techniques can be used for MMT. The proof-of-  
224 concept of MMT (de Groot et al., 2018) was provided using a SSM, here we present MMT  
225 results based on MTJ and QDM measurements.

226 **2.2.1 Scanning SQUID set-ups**

227 In scanning SQUID microscopy a SQUID (Superconducting QUantum Interference  
 228 Device) sensor is used to measure magnetic fields above a sample. A SQUID sensor that  
 229 consists of a superconducting loop containing Josephson junctions hovers over (or is in  
 230 contact with) a sample and measures the component of the magnetic flux density per-  
 231 pendicular to its surface (Kirtley & Wikswo, 1999; Reith et al., 2017). SQUID sensors  
 232 in SSM set-ups can attain effective magnetic moment sensitivities in the order of  $10^{-16}$   
 233  $\text{Am}^2$  and are therefore the most sensitive magnetometers to date. This makes them the-  
 234oretically very suitable for MMT analyses. It is the requirement of superconductivity,  
 235 however, that puts constraints on the usefulness of scanning SQUID set-ups for MMT.

236 In the SSM set-up used for the proof-of-concept of MMT (de Groot et al., 2018)  
 237 the sample was submerged with the SQUID sensor in liquid helium. This allows the SQUID  
 238 sensor to be in contact with the sample and the sample-sensor distance to be in the or-  
 239 der of just 1-2  $\mu\text{m}$ . This allows for a spatial resolution in the order of  $\sim 1 \mu\text{m}$ , hence this  
 240 SSM set-up can exploit the full native sensitivity of SQUID sensors at unsurpassed spa-  
 241 tial resolution. Nevertheless, the sample is measured at a temperature of  $\sim 4 \text{ K}$  – far  
 242 below its Verwey transition. Therefore this set-up impedes determining magnetizations  
 243 of naturally occurring magnetic states in a sample at room temperature and is therefore  
 244 of limited use for paleomagnetic and rock-magnetic applications of MMT.

245 In other SSM set-ups previously used for paleomagnetic or rock-magnetic appli-  
 246 cations the SQUID sensor is thermally isolated from the sample (e.g.: Egli & Heller, 2000;  
 247 Fong et al., 2005; Weiss et al., 2007; Lima & Weiss, 2016; Oda et al., 2016). This can  
 248 only be attained by increasing the sample-sensor distance, in the most recent set-ups this  
 249 distance can be as little as 200  $\mu\text{m}$  (Oda et al., 2016); hence the spatial resolution limit  
 250 of such set-ups is in the order of 200  $\mu\text{m}$ . In spite of the major technical achievement to  
 251 thermally isolate the sample at room temperature from the SQUID sensor at  $\sim 4 \text{ K}$  over  
 252 just 200  $\mu\text{m}$ , the spatial resolution does not allow for a reliable magnetic inversion for  
 253 individual grains in natural samples given the concentration of magnetic grains. There-  
 254 fore also the thermally isolated SSM set-ups seem unsuitable for MMT, even consider-  
 255 ing their unsurpassed magnetic sensitivity.

### 256 **2.2.2 Magnetic Tunnel Junction scanners**

257 Advances in non-cryogenic scanning magnetometry sensors have led to the devel-  
258 opment of Magnetic Tunnel Junction (MTJ) sensors that are suitable for paleomagnetic  
259 and rock-magnetic applications (Lima et al., 2014). MTJ sensors exploit a quantum phys-  
260 ical effect by which electrons can tunnel through an ultra-thin insulating layer that is  
261 in between two ferromagnetic layers, creating a small current through the sensor. This  
262 tunneling effect is governed by the magnetization in the two ferromagnetic layers of the  
263 sensor. Therefore the tunneling current, and hence the resistance of the sensor, changes  
264 due to variations in the external magnetic field. The major advantage of these MTJ sen-  
265 sors over typical SQUID sensors is that MTJ sensors operate at room temperature, this  
266 makes the expensive and complex cryogenic systems for SSM set-ups superfluous. Nev-  
267 ertheless, typical MTJ sensors are  $> 4$  orders of magnitude less sensitive compared to  
268 SQUID sensors (Lima et al., 2014). This major setback in sensitivity is only partially  
269 compensated by the smaller sample-sensor distances that are possible in MTJ set-ups  
270 (down to  $\sim 7 \mu\text{m}$ ). This results in typical effective magnetic moment sensitivities in the  
271 order of  $10^{-14} \text{ Am}^2$  for the most advanced MTJ set-ups (Lima et al., 2014). The spa-  
272 tial resolution of an MTJ set-up primarily depends on the actuators used to move the  
273 sensor or sample, and is often in the order of  $5 - 10 \mu\text{m}$ .

274 The sensitivity of the surface magnetometry technique is not a major concern when  
275 making scans of synthetic or volcanic material. For the proof-of-concept of MMT (de Groot  
276 et al., 2018), the sensitivity of the SSM set-up had to be reduced in favor of dynamic range  
277 to properly image the magnetization of the sample. This makes MTJ-based set-ups the-  
278 oretically very suitable for MMT analyses, primarily because of their small sample-sensor  
279 distance and high spatial resolution. In this study we obtained a magnetic surface scan  
280 of the same synthetic sample that was used in de Groot et al. (2018), on the MTJ set-  
281 up at the University of Cambridge.

### 282 **2.2.3 Quantum Diamond Microscope**

283 Recently, an entirely new type of scanning magnetometry was optimized for geo-  
284 logical samples: the Quantum Diamond Microscope (QDM) (Glenn et al., 2017; Farchi  
285 et al., 2017; Levine et al., 2019; Fu et al., 2020). The QDM uses optical fluorescence in  
286 nitrogen-vacancy (NV) centers in a diamond chip to determine the magnetic field above

287 a sample. The magnetic fields are thus derived from an optical image, hence its theo-  
288 retical spatial resolution limit is determined by the diffraction limit of the optics. The  
289 wavelength of the fluorescence is 600-800 nm; the theoretical limit for the spatial reso-  
290 lution therefore is  $\sim 350$  nm, depending on the quality of the optical path (Levine et  
291 al., 2019). In practice, however, current set-ups attain a spatial resolution of  $1.2 \mu\text{m}$  (Glenn  
292 et al., 2017). The sensitivity of the QDM depends on several variables, e.g. the time over  
293 which the measurements are done, the thickness of the layer of NV centers in the dia-  
294 mond, and the characteristics of the optical components used. In general, the sensitiv-  
295 ity of the QDM may be expected to be better than the sensitivity of MTJ sensors, but  
296 does not attain the sensitivity of SQUID sensors (Glenn et al., 2017).

297 An important property and possible draw-back of the QDM for MMT applications  
298 is that it needs a bias field to operate (Glenn et al., 2017). During normal operation this  
299 bias field is approximately 0.9 mT and its polarity is switched many times. This enables  
300 discriminating between remanent (i.e. ferrimagnetic) and paramagnetic/viscous mag-  
301 netizations. The QDM produces two maps: one of the remanent magnetizations that in-  
302 herently misses the remanence carried by grains with a coercivity below the bias field;  
303 and another with the induced magnetizations by the bias field. Since the iron-oxide grains  
304 that carry information on the past state of the Earth's magnetic field generally have co-  
305 ercivities higher than the bias field currently used (0.9 mT), this property of the QDM  
306 does not jeopardize the paleomagnetic interpretation of QDM results. But for some rock-  
307 magnetic applications such as magnetic viscosity studies, however, this bias field needs  
308 to be considered.

309 Since the QDM is theoretically very suitable for MMT analyses, we obtained a mag-  
310 netic surface scan of the same synthetic sample used for the MTJ analysis and for the  
311 proof-of-concept of MMT (de Groot et al., 2018) at the QDM set-up at Harvard Uni-  
312 versity. Furthermore, we obtained a magnetic surface scan from a natural volcanic sam-  
313 ple.

### 314 **2.3 Co-registration**

315 The two data-sets for MMT, the spatial information on the iron-oxide grains from  
316 the microCT analysis and the magnetic surface scan, must be co-registered in the same  
317 coordinate system for a reliable inversion. This co-registration consists of a 'mapping'

318 of the magnetic surface scan in the  $x$  and  $y$ -coordinates of the microCT data, and de-  
 319 termining the sample-sensor distance, or scan height, the  $z$ -coordinate. For the SSM and  
 320 MTJ data the locations of the iron-oxides closest to the surface as produced by the mi-  
 321 croCT scan are manually aligned with the largest magnetic anomalies present in the mag-  
 322 netic surface scan. Since the QDM is an optical acquisition technique, it is possible to  
 323 make an optical image of the surface of the sample in exactly the same coordinates as  
 324 the magnetic scan is made in. This greatly eases the tedious, manual process of map-  
 325 ping the two data-sets.

326 The sample-sensor distance, or scan-height, is often even more difficult to deter-  
 327 mine. But, since magnetic moments decay with the third power of distance, it is of ut-  
 328 most importance to have a good estimate of this parameter. The SSM sensor in the proof-  
 329 of-concept was in contact with the sample, hence the sample-sensor distance can be es-  
 330 timated with precision. For the MTJ and QDM set-ups this distance is derived from the  
 331 actuators that are used to move the sensor (MTJ), or the sample (QDM), and may be  
 332 less precise, depending on the actuators used.

## 333 2.4 Inversion

334 The combination of microCT data and magnetic surface scans enables to uniquely  
 335 reconstruct the magnetic moments of individual iron-oxide grains in a sample, provided  
 336 that they are spatially sufficiently separated. A grain is defined as a group of intercon-  
 337 nected voxels in the microCT scan; each grain is considered to be uniformly magnetized.  
 338 For the inversion each grain is mathematically isolated inside a small sphere  $\Omega^i$ ,  $i = 1 \dots N$ .  
 339 These spheres cannot intersect, i.e. they are pairwise disjoint. This implies that when  
 340 grains are spatially not sufficiently separated, or when grains are intertwined, these grains  
 341 can only be placed inside a sphere together and their magnetic moment is solved for as  
 342 one. A number  $N$  spheres  $\Omega^i$  are now considered to be magnetic source regions inside  
 343 a larger sphere  $\Omega$ . In a slightly simplified version, the underlying theorem for the inver-  
 344 sion (Fabian & de Groot, 2019) guarantees that the radial magnetic field component  $B_r^\Omega$   
 345 on the sphere  $\Omega$  uniquely defines the radial field components  $B_r^i$ ,  $i = 1 \dots N$ , on the  
 346 surfaces of all of the  $N$  inner spheres  $\Omega^i$  (Fabian & de Groot, 2019). To apply this the-  
 347 orem in practice, all magnetic sources in a sample have to be identified, and placed into  
 348  $N$  pairwise separate spheres, such that each magnetic grain lies completely inside one  
 349 of these spheres, and no magnetic sources are outside them. It is then theoretically pos-

350 sible to identify the magnetic dipole moment of each of the  $N$  spheres from a precise mea-  
 351 surement of  $B_r^\Omega$  on a spherical surface around all  $N$  spheres.

352 In practice, the magnetic scanning measurement is performed at finitely many po-  
 353 sitions on a sufficiently large rectangular planar region  $R \subset \Omega$  above the sample. This  
 354 rectangle mathematically corresponds to a fraction of an infinitely large sphere, which  
 355 is chosen large enough, such that the field component  $B_r^\Omega$  outside  $R$  is negligibly small.  
 356 Conceptually, the inversion proceeds through the following steps:

- 357 1. Define the scan surface  $R$  and the centers and sizes of the  $N$  spheres  $c_i$ ,  $i = 1 \dots N$   
 358 that contain all sources. These spheres are determined by assuming that all mag-  
 359 netic sources are identified by density anomalies in the microCT data.
- 360 2. Measure  $B_r^\Omega$  on  $R$  with sufficient resolution and accuracy.
- 361 3. Use the unique continuous (Fabian & de Groot, 2019) inversion operator

$$B_r^\Omega \rightarrow B_r^i$$

362 to calculate the radial component on the surface  $\Omega^i$  of the  $i$ -th sphere.

- 363 4. Decompose  $B_r^i$  in spherical harmonics to isolate its dipole moment  $m_i$ .

364 This conceptual procedure shows that in case of sufficient accuracy and resolution the  
 365 dipole moments  $m_i$  are uniquely defined, and can be recovered with arbitrary precision.  
 366 Because the recovery essentially involves a downward continuation of the radial field from  
 367 the larger sphere  $B_r^\Omega$  to each smaller sphere  $B_r^i$ , it substantially amplifies noise and re-  
 368 quires extremely precise and accurate data to succeed (e.g. Blakely, 1996).

#### 369 **2.4.1 Inversion routine**

370 The practical inversion routine used here is described in de Groot et al. (2018). It  
 371 exploits the more detailed geometric information from the microCT to obtain a repre-  
 372 sentation of the shapes of individual grains as a union of a small number of rectangu-  
 373 lar boxes (i.e. cuboids). Each grain  $P_i$ ,  $i = 1, \dots, N$ , is described as a union of  $n_j$  cuboids  
 374  $C_{i,j}$  with  $j = 1, \dots, n_j$ , each of which is homogeneously magnetized with magnetiza-  
 375 tion  $M_i$ . For each scanning point  $r_k$ ,  $k = 1 \dots K$  the forward model equation calcu-  
 376 lates the magnetic flux through the sensor on the surface of the sample generated by each  
 377 cuboid  $C_{i,j}$  as function of its magnetization vector  $\mathbf{M}_i = (M_{i,1}, M_{i,2}, M_{i,3})$ . The sum

378 provides the total flux  $F_k$  as a linear function of the  $3N$  parameters defining all vectors  
 379  $\mathbf{M}_i$ . Thereby the forward model defines a  $K \times 3N$  design matrix  $\mathbf{A}$  which transforms  
 380 the vector

$$\mathbf{v} = (M_{1,1}, M_{1,2}, M_{1,3}, M_{2,1}, M_{2,2}, M_{2,3}, \dots, M_{N,2}, M_{N,3})$$

381 into the measured flux signals

$$\mathbf{F} = (F_1, F_2, F_3, \dots, F_K),$$

382 according to the forward equation

$$\mathbf{F} = \mathbf{A} \mathbf{v}.$$

383 The inversion is performed by calculating the Moore-Penrose pseudoinverse  $\mathbf{A}^+$  (Moore,  
 384 1920; Penrose, 1955) and applying this to the vector  $\mathbf{F}_{\text{MMT}}$  of the measured values of  
 385  $F_k$  via

$$\mathbf{v}_0 = \mathbf{A}^+ \mathbf{F}_{\text{MMT}}.$$

386 By definition of the pseudoinverse, for  $K > 3N$  this returns the vector  $\mathbf{v}_0$  of all  
 387 magnetizations for the least-square fit of the measured values by assuming a homoge-  
 388 neous magnetization for each grain.

389 Due to the geometrical approach of this routine, it produces magnetizations of the  
 390 grains, i.e. volume normalized magnetic moments. In contrast to magnetic moments, these  
 391 magnetizations are prone to uncertainties arising from the microCT data processing, such  
 392 as resolution limits, thresholding and voxel binarizations. Multiplying the magnetiza-  
 393 tions by the same volumes that were used in the inversion procedure yield the magnetic  
 394 moments of the grains that explain the observed magnetic anomalies in the magnetic sur-  
 395 face scan best. These magnetic moments are insensitive to the uncertainties in the vol-  
 396 ume estimates associated with the microCT data processing.

397

## 2.5 Residuals

398

399

400

401

402

403

404

405

406

407

408

The accuracy of the inversion can be assessed by calculating the residuals left by the inversion. This is done by assigning all grains their calculated magnetic moment and running a forward model to determine the resulting magnetic map on the surface of the sample. This calculated magnetic surface map is then subtracted from the actual, measured, magnetic surface scan. This produces a map of the residuals after the inversion, i.e. a map of the measured magnetic flux on the surface that is not explained by the calculated magnetic moments of the grains. After an accurate inversion we expect low residuals; high magnetic anomalies in the residuals often arise from larger grains close to the surface. Their magnetic expressions on the surface of the sample are generally more complex due to their complex magnetic domain states. Therefore these magnetic anomalies cannot be explained by our assumption of dipolar magnetic moments in the grains.

409

## 3 Obtaining magnetic directions from MMT

410

411

412

413

414

415

416

To obtain a magnetic direction from magnetizations of individual grains as produced by our inversion routine (section 2.4.1), we first determine the magnetic moments ( $\mathbf{m}$ , in  $\text{Am}^2$ ) of the individual grains by multiplying their calculated magnetizations ( $\mathbf{M}$ , in  $\text{A/m}$ ) by their volume. We also change the mathematical indices 1, 2, 3 describing the axes of the coordinate system used in section 2.4 to the axes they physically represent:  $x, y, z$ ; with the x-y-plane as the surface of the sample and  $z$  going down into the sample from its surface. The total magnetic moment of the grain is then given by:

$$m_{\text{grain}} = \sqrt{m_x^2 + m_y^2 + m_z^2}$$

417

418

419

420

The magnetic direction is defined by a declination and inclination with respect to the coordinate system of the sample. The declination is defined as the angle with the positive x-axis of the sample in the x-y-plane; the inclination is defined as the smallest angle with the positive z-axis of the sample:

$$\text{dec} = \arctan(m_x/m_y) \quad \text{and} \quad \text{inc} = \arcsin(m_z/m_{\text{grain}})$$

**Table 1.** Details of the MMT inversions

	synthetic sample		volcanic sample			
	area 1	area 2	area 3	area 4	area 3	area 4
scanning technique	MTJ	QDM	QDM	QDM	QDM	QDM
sensor geometry	ellipse <sup>a</sup>	square	square	square	square	square
sensor surface ( $\mu\text{m}^2$ )	8.0	1.44	1.44	1.44	1.44	1.44
datapoints (x, y)	91×96	170×166 <sup>b</sup>	126×126	209×230	167×138	184×130
scan height ( $\mu\text{m}$ )	33.56	6.0	6.0	6.0	6.0	6.0
step size ( $\mu\text{m}$ )	10.0	6.0 <sup>b</sup>	1.2	1.2	1.2	1.2
<b>magnetic scan</b>						
<b>spatial information</b>						
microCT resolution ( $\mu\text{m}$ )	0.714	0.714	0.675	0.675	0.675	0.675
microCT voxel size ( $\mu\text{m}^3$ )	0.36	0.36	0.31	0.31	0.31	0.31
scan dimensions (x, y, z; $\mu\text{m}$ )	910×960×50	1020×996×50	150×150×30	250×275×30	200×165×30	220×155×30
number of grains	128	128	11	42	18	20
number of cuboids	19,552	19,552	305	1,192	388	555
grain concentration (grains/ $\text{mm}^3$ )	2,930	2,520	16,300	20,360	18,180	19,550

<sup>a</sup> modelled as a square of  $2.83 \times 2.83 \mu\text{m}$ <sup>b</sup> after subsampling the original QDM scan which has a step size of  $1.2 \mu\text{m}$

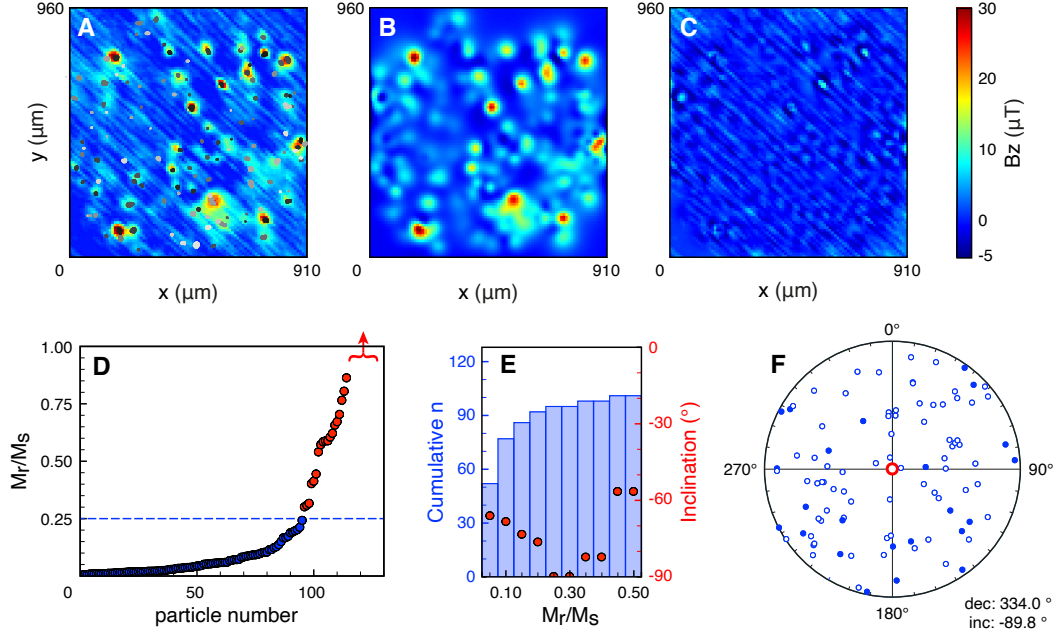


**Figure 2.** Results of MTJ experiments on the synthetic sample. The 128 grains in the sample are superimposed on the MTJ measurements (in gray-scale, A). The outcome of the forward calculations is in B, the map of the residuals is in C. The theoretical remanence ratios ( $M_r/M_s$ ) of the individual magnetite grains (see main text) are sorted in increasing order (D). The graph is clipped at the theoretical maximum  $M_r/M_s$  ratio of 1; 14 grains with  $M_r/M_s$  ratios between 1.08 and 9.45 are not shown, indicated by the red arrow. For cumulative bins of  $M_r/M_s$  ratios the cumulative  $n$  is plotted together with the resulting inclination for the selected grains (E). For grains with  $M_r/M_s$  ratios  $< 0.25$  (blue dashed line in D), the resulting direction differs just  $0.2^\circ$  from the expected direction. For these grains the distribution of their individual directions is in F (open symbols pointing upwards, closed symbols downwards), with the resulting direction in red.

421 To calculate the bulk magnetization for the entire sample based on all grains or a  
 422 sub-set of grains, first the  $m_x$ ,  $m_y$ , and  $m_z$  components of the selected grains are summed  
 423 into  $\Sigma m_x$ ,  $\Sigma m_y$ , and  $\Sigma m_z$ . Then these parameters are used in the equations above.

### 424 3.1 A magnetic direction from an MTJ scan

425 To obtain a magnetic direction using MMT we used the same synthetic sample as  
 426 used in de Groot et al. (2018). This sample contains 128 magnetite grains with diam-  
 427 eters ranging from 5 to 35  $\mu\text{m}$  that are randomly distributed in space (Supplementary

428 movie 1). First, we gave it an Isothermal Remanent Magnetization (IRM) with a pulsed  
429 magnetic field of 1 T perpendicular to the surface of the sample, to give the sample a  
430 known magnetic state by suspending the sample in a Lakeshore Vibrating Sample Mag-  
431 netometer at the University of Cambridge and briefly switching on the field. The sam-  
432 ple was scanned in the MTJ set-up at the University of Cambridge directly after giving  
433 the sample its IRM. The entire surface of the sample was scanned with a step size of 10  
434  $\mu\text{m}$ , yielding 8736 data points, with a scan height of 33.56  $\mu\text{m}$  (Table 1). The scan shows  
435 some scanning artifacts in the scan direction, identified as diagonal stripes (Fig. 2A).  
436 The MTJ scan shows large positive magnetic anomalies, up to  $> 30 \mu\text{T}$ , and much smaller  
437 negative anomalies, down to  $< -5 \mu\text{T}$ . This differs from the observations in de Groot  
438 et al. (2018), where the positive and negative magnetic anomalies seem more symmet-  
439 rical distributed around 0  $\mu\text{T}$ . This can be explained by the much larger scan height used  
440 in the MTJ scan: 33.56  $\mu\text{m}$  vs 2  $\mu\text{m}$  for the SSM set-up used in de Groot et al. (2018).  
441 Since the scanner is further away from the magnetic sources, the magnetic expression  
442 of the sources represent more their ‘far-field’ (i.e. dipolar) nature. Moreover, the MTJ  
443 scan was made after giving the sample an IRM, while the magnetic states in de Groot  
444 et al. (2018) represent a more natural magnetic state. Hence the grains were much stronger  
445 and more uniformly magnetized during the MTJ scan.

446 The co-registration between the MTJ and microCT results was done manually by  
447 aligning the locations of the grains closest to the surface to the strongest magnetic anoma-  
448 lies in the MTJ scan (Fig. 2A). The co-registration was accurate and allowed for a proper  
449 inversion; magnetizations were obtained for all 128 grains in the synthetic sample (Sup-  
450 plemental Table 1). The results of the inversion were used as input for a forward model  
451 (Fig. 2B) which yields a close representation of the magnetic surface scan (Fig. 2A). This  
452 leads to generally very low residuals (Fig. 2C). The diagonal scanning artifacts in the  
453 MTJ scan are the most prominent feature in the residuals, hence the inversion is insen-  
454 sitive to these, and they are not propagated into the calculated magnetizations per grain.

455 From this dataset alone it is difficult to label magnetizations of individual grains  
456 ‘reliable’ or ‘unreliable’. In the future, this could be done by e.g. determining the mag-  
457 netizations of individual grains after series of magnetic treatments. Nevertheless it is pos-  
458 sible to provide a first-order assessment of the accuracy of the magnetizations produced  
459 here by considering the theoretical remanence ratios ( $M_r/M_s$ ) of the individual grains.  
460 These can be estimated by dividing the remanent magnetization ( $M_r$ ) of the individual

461 grains as produced by the inversion, by their theoretical saturated magnetization ( $M_s$ )  
 462 (Fig. 2D). Since the grains in the synthetic sample are pure magnetite grains, their the-  
 463 oretical saturation magnetization is  $480 \text{ kAm}^{-1}$  (Dunlop & Özdemir, 1997). It is impor-  
 464 tant to note that we use the volume estimates of the grains as produced by the microCT  
 465 analysis to determine both the  $M_r$  and  $M_s$  values. The uncertainties associated with the  
 466 manual tresholding and voxel binarizations during microCT data interpretation there-  
 467 fore propagate into the calculated magnetizations. Nevertheless, the volumes for all grains  
 468 were obtained in a single workflow using one threshold. Since our analysis based on the  
 469  $M_r/M_s$  ratios is comparative in nature the absolute uncertainties in volume estimates  
 470 are somewhat suppressed in our analysis. Moreover, the resulting magnetic directions  
 471 for subsets of grains in the sample are based on the individual magnetic moments of grains  
 472 that are insensitive to the uncertainties in the volume estimates.

473 Most grains have low  $M_r/M_s$  ratios, as expected since the grains in the synthetic  
 474 sample have diameters ranging from  $5\text{--}35 \mu\text{m}$ . Some grains, however, have  $M_r/M_s$  ra-  
 475 tios that are much larger than expected, i.e. well above 0.5, and some  $M_r/M_s$  ratios are  
 476 even higher than the theoretical limit of 1. For these grains it is most likely that the in-  
 477 version did not produce accurate estimates of the magnetization, and they should be ex-  
 478 cluded from calculating the magnetic direction for the entire sample. Besides this the-  
 479 oretical maximum, there is no theoretical value for the cut-off for the  $M_r/M_s$  ratios to  
 480 select the grains that should be included in calculating the magnetic direction. We there-  
 481 fore took an iterative approach to select the grains based on their  $M_r/M_s$  ratios that yield  
 482 a resulting magnetic direction closest to the applied magnetic field. Furthermore the re-  
 483 sulting direction should be insensitive to the addition of small numbers of grains to the  
 484 ensemble - i.e. adding one or two grains should not have a major effect on the result-  
 485 ing direction. Since we know that the expected paleodirection is perpendicular to the  
 486 surface we expect an inclination of  $-90^\circ$ , with any value for the declination. We calcu-  
 487 lated the magnetic direction for grains based on their  $M_r/M_s$  ratio, starting with grains  
 488 with  $M_r/M_s$  ratios  $\leq 0.05$ . We then added grains based on their  $M_r/M_s$  ratio in bins  
 489 of 0.05, until the  $M_r/M_s$  ratio reached 0.5. This results in pairs of number of grains in-  
 490 cluded ( $n$ ) and the resulting inclination (Fig. 2E). For the grains with  $M_r/M_s$  ratios  $\leq$   
 491  $0.25$ , the resulting inclination is  $-89.8^\circ$ , with a declination of  $334.0^\circ$ . This is just  $0.2^\circ$   
 492 off of the expected direction (Fig. 2F). For the next bin, with  $M_r/M_s$  ratios  $\leq 0.35$  (the  
 493 bin between 0.25 and 0.30 has no additional grains), three additional grains are included

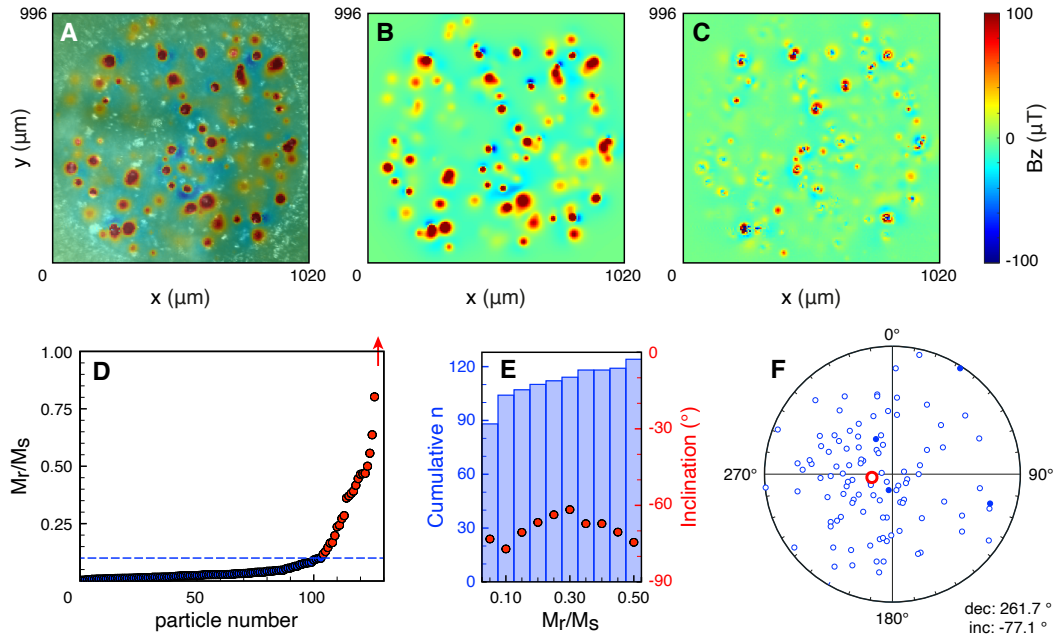


**Figure 3.** Results of QDM experiments on the synthetic sample. The optical microscopy image is in the background in gray-scale (A), the map of the magnetic flux density perpendicular to the surface (in color) is super-positioned with 50% transparency. The outcome of the forward calculations is in B, the map of the residuals is in C. The theoretical  $M_r/M_s$  ratios of the individual magnetite grains (see main text) are sorted in increasing order (D). The graph is clipped at the theoretical maximum  $M_r/M_s$  ratio of 1; one grain with a  $M_r/M_s$  ratio of 2.42 is not shown, as indicated by the red arrow. For cumulative bins of  $M_r/M_s$  ratios the cumulative  $n$  is plotted together with the resulting inclination for the selected grains (E). For grains with  $M_r/M_s$  ratios  $< 0.10$  (blue dashed line in D), the resulting direction is closest to the expected direction. For these grains the distribution of their individual directions is in F (open symbols pointing upwards, closed symbols downwards), with the resulting direction in red.

494 in calculating the magnetic direction. These three grains have a large influence on the  
 495 resulting inclination, making the resulting direction very sensitive to individual grains  
 496 and therefore unstable (Fig. 2E). Moreover,  $M_r/M_s$  ratios up to 0.25 are plausible for  
 497 grains with diameters ranging from 5–35  $\mu\text{m}$  (e.g.: de Groot, Dekkers, et al., 2014; Mon-  
 498 ster et al., 2018).

### 499 3.2 A magnetic direction from a QDM scan

500 To test the performance of MMT using different magnetic surface scanning tech-  
 501 niques we repeated the experiment with the MTJ using the QDM at Harvard Univer-  
 502 sity (Table 1). We used the same synthetic sample again, and gave it a 1 T IRM field  
 503 perpendicular to its surface using an ASC Impulse Magnetizer (IM-10-30) at Massachusetts  
 504 Institute of Technology. The magnetic surface scans were made the same day. Since the  
 505 QDM also produces an optical image of the sample in the same coordinate system as the  
 506 magnetic scan, the mapping between the QDM scan and the spatial data from the mi-  
 507 croCT scan was relatively easy (Fig. 3A). The sample-sensor distance in the QDM is much  
 508 smaller compared to the MTJ scan, the magnetic anomalies are therefore larger ( $\sim 100$   
 509  $\mu\text{T}$  for the QDM, compared to  $\sim 30 \mu\text{T}$  for the MTJ). The inversion yielded magneti-  
 510 zations for all 128 grains in the sample (Supplemental Table 2). These magnetizations  
 511 were used to make a forward calculation of the surface magnetization (Fig. 3B), and a  
 512 map of the residuals left by the inversion (Fig. 3C). The residuals are low, although there  
 513 are prominent and complex anomalies over some grains, usually grains closer to the sur-  
 514 face. These observations are explained by the smaller sample-sensor distance of the QDM  
 515 compared to the MTJ: complex, non-dipolar, structures are only observed in close prox-  
 516 imity of the grains. To interpret the resulting magnetic direction for the entire sample  
 517 we followed the same workflow as for the MTJ scan. First, the  $M_r/M_s$  ratios were cal-  
 518 culated for the individual grains using their theoretical  $M_s$  of  $480 \text{ kAm}^{-1}$ . More than  
 519 100 grains have an  $M_r/M_s$  ratio  $< 0.10$ . Since we used the same grain volumes for the  
 520 MTJ and QDM data analyses, this implies that the magnetizations of the grains (and  
 521 hence their  $M_r/M_s$  ratios) from the QDM scan are generally somewhat lower than those  
 522 from the MTJ scan (Fig. 3D). Again, we use bins of 0.05 for the  $M_r/M_s$  ratios and cal-  
 523 culate the resulting inclination (Fig. 3E). For the set of grains with  $M_r/M_s$  ratios be-  
 524 tween 0 and 0.10 the inclination is  $-77.1^\circ$ , this is closest to the expected inclination of  
 525  $-90^\circ$  for any of the  $M_r/M_s$  ratio bins up to 0.5, but still  $-12.9^\circ$  off. The declination  
 526 for this resulting direction is  $261.7^\circ$ . Furthermore, the number of grains with a direc-  
 527 tion in the upper hemisphere (i.e. with a direction more than  $90^\circ$  off of the applied mag-  
 528 netic field) is 24 for the MTJ experiment and only 4 for the QDM experiment (compare  
 529 Figs. 2F and 3F). This implies that the distribution of the directions of the individual  
 530 grains seems narrower for the results using the MTJ scanner compared to the QDM re-  
 531 sults.

532 It is currently difficult to explain the differences between the MTJ and QDM stud-  
533 ies using the same sample and magnetic treatment in more detail. These differences may  
534 have experimental reasons, e.g. the smaller sample-sensor distance in the QDM leads to  
535 detecting more complex magnetic signals and our assumption to solve for dipolar mag-  
536 netizations may be violated. Furthermore, the IRM imparting field was applied directly  
537 preceding the MTJ scan at the University of Cambridge; while for the QDM experiment  
538 the sample had to be transported from Massachusetts Institute of Technology to Har-  
539 vard. Although the sample was measured on the QDM within hours after applying the  
540 IRM, the additional time and handling of the sample before the QDM scan might have  
541 given potential viscous processes more time to evolve. There can also be a rock-magnetic  
542 reason for the observed differences: the coercivities of some grains may be (partially) very  
543 low, so their signal would be (partially) canceled by the switching bias field applied in  
544 the QDM (0.9 mT), leading to lower total magnetizations in the QDM experiment. Nev-  
545 ertheless, it is encouraging to see that the resulting magnetic directions from both the  
546 MTJ and QDM experiments are close to the expected direction, and that it is possible  
547 to select and consider the contributions of individual grains in a sample.

#### 548 **4 Rock-magnetic information from a volcanic sample**

549 The concentration of magnetic grains in the synthetic sample is about one order  
550 of magnitude lower than the concentration of magnetic grains in naturally occurring lavas  
551 (Table 1). To test whether MMT is also capable of determining magnetizations of in-  
552 dividual grains in a natural sample we subjected a Hawaiian lava to an MMT study. We  
553 drilled a small core with a diameter of 3 mm from a standard thin section with a sam-  
554 ple thickness of 30  $\mu\text{m}$  from the 1907 flow of the Kilauea (site HW03 from de Groot et  
555 al. (2018)). Our sample was taken from the same paleomagnetic drill core as the sam-  
556 ple used in ter Maat et al. (2018) where the chemical, physical, and magnetic states of  
557 several individual iron-oxide grains were thoroughly assessed with e.g. Scanning Elec-  
558 tron Microscopy, Electron Back-Scatter Diffraction, Magnetic Force Microscopy, and Micro-  
559 probe analyses. The sample was polished using a colloid silica suspension prior to the  
560 magnetic scans to remove surface magnetizations due to mechanical polishing (see Sup-  
561plementary Fig. 9 in de Groot, Fabian, et al. (2014)). The magnetic surface scan was  
562 made with the QDM at Harvard University. We did not apply any magnetic treatment  
563 to the sample beforehand; the magnetizations of the grains therefore most likely resem-

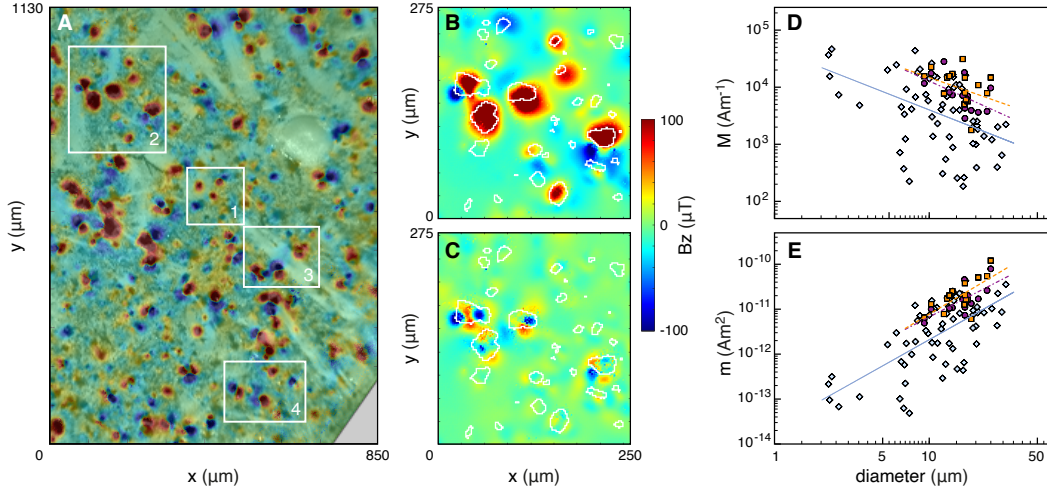


**Figure 4.** Results of QDM experiments on a volcanic sample (HW03, see main text). The optical microscopy image is in the background in gray-scale (A), the map of the magnetic flux density perpendicular to the surface (in color) is super-positioned with 50% transparency. The QDM data of area 2 (A) is in B, with the outlines of the iron-oxide grains as identified by microCT in white. The residual after the inversion to produce the individual magnetic moments per grain (C) are generally low and non-uniform, indicating a proper inversion result. The magnetizations (D) and magnetic moments (E) of grains with  $M_r/M_s$  ratios  $\leq 0.10$  (see main text) are plotted as function of their diameter as blue diamonds, with their linear trend line in blue. The results of de Groot et al. (2018) are also included for comparison: the magnetizations arising from a 'natural magnetic state' in purple circles / dashed trend line, and the magnetizations after applying an Anhyseretic Remanent Magnetization (ARM) with a bias field of  $40 \mu\text{T}$  in orange squares / dashed trend line.

564 ble a natural magnetic state. The iron-oxide grains in the sample were obtained from  
565 a microCT scan done at the Nanotom-S at TU Delft. The spatial resolution in this scan  
566 is  $\sim 0.7 \mu\text{m}$ .

567 We used the optical image of the QDM to map the magnetic surface scan on the  
568 spatial data of the iron-oxide grains obtained by the microCT scan. To reduce compu-  
569 tation time the inversions were done for four small areas of the sample (Fig. 4A). We  
570 obtained magnetizations for all 91 grains inside the four areas. The residuals left by the  
571 inversion are low compared to the residuals reported for the synthetic sample (Fig. 4C),  
572 and are again dominated by complex magnetizations arising from grains close to the sur-  
573 face of the sample.

574 To assess the reliability of the inversion results we again calculated the theoret-  
575 ical  $M_r/M_s$  ratio for each grain, using the  $M_s$  of pure magnetite. The naturally occur-  
576 ring grains in Hawaiian lavas are generally rich in Ti; Curie balance experiments on sis-  
577 ter samples from site HW03 exhibit a gradual decay of the magnetization with temper-  
578 ature, with Curie temperatures around 250 and 450°C that are not very well expressed  
579 (de Groot et al., 2013; ter Maat et al., 2018). Replacing Fe by Ti in the iron-oxide solid  
580 solutions lowers the  $M_s$  values (Readman & O'Reilly, 1972; Dunlop & Özdemir, 1997).  
581 It is therefore safe to assume that the  $M_s$  of pure magnetite is overestimating the real  
582  $M_s$  value for most of the grains in the sample, leading to artificially low  $M_r/M_s$  ratios  
583 for our volcanic sample.

584 From the 91 grains in the inversions, 16 grains have  $M_r/M_s$  ratios higher than the  
585 theoretical maximum of 1. These grains were thus not properly resolved by the inver-  
586 sion and were rejected. Building on the experience with the QDM results for the syn-  
587 thetic sample and given that the  $M_s$  value for magnetite is overestimating the true  $M_s$   
588 values for our grains, we deem the grains with  $M_r/M_s$  ratios  $>0.10$  suspect. These grains  
589 are not considered further in our analyses. This leaves 62 grains for which the magne-  
590 tizations are now known. These magnetizations are plotted against the diameters of the  
591 grains that are obtained from the microCT analysis (Fig. 4D). Since the volume of the  
592 grains is known, their magnetic moments can be calculated and plotted as function of  
593 their diameter as well (Fig. 4E).

594 The natural sample was not magnetically treated prior to the QDM measurements,  
595 the magnetizations are therefore most likely resembling a natural magnetic state. In de

596 Groot et al. (2018) the pure magnetite grains in the synthetic sample were also either  
597 untreated prior to the SSM measurements (in purple in Fig. 4D and E), or analyzed af-  
598 ter applying an Anhysteretic Remanent Magnetization (ARM) with a bias field of 40  $\mu\text{T}$   
599 to the sample (in orange in Fig. 4D and E). The magnetic states in de Groot et al. (2018)  
600 therefore also resemble a natural magnetic state and can be meaningfully compared to  
601 the magnetic states of our natural sample. The magnetizations of the grains in the nat-  
602 ural sample are on average lower than the magnetizations for the synthetic sample. This  
603 is explained by the grains being enriched in Ti in the natural sample, lowering their mag-  
604 netizations. The trends in magnetization and magnetic moment as function of diame-  
605 ter, however, are remarkably similar for the natural sample compared to the trends re-  
606 solved for the pure magnetite grains in de Groot et al. (2018).

## 607 **5 Discussion**

608 Building on the proof-of-concept of MMT (de Groot et al., 2018), we showed that  
609 it is possible to obtain a magnetic direction from a subset of grains in a synthetic sam-  
610 ple, and derive magnetic information from individual grains in natural volcanic sample.  
611 Here we will first discuss the technical characteristics and limitations of MMT, and then  
612 its potential for both paleomagnetism and rock-magnetism.

### 613 **5.1 Spatial characterization of the grains**

#### 614 **5.1.1 Detecting all iron-oxides**

615 The spatial characteristics of all iron-oxide grains in the sample are determined from  
616 a microCT scan. For a reliable inversion it is important that all magnetic sources are  
617 properly identified, otherwise not all magnetic surface anomalies can be attributed to  
618 their source. Being able to detect all potentially magnetic iron-oxides depends on select-  
619 ing the proper threshold in the microCT scan above which grains are deemed iron-oxides,  
620 and the resolution of the microCT scan. Since the iron-oxides have a distinct density con-  
621 trast to most other minerals present in volcanic samples, and also to artificial matrices  
622 such as epoxy, the attenuation spectrum from the microCT scan is often bi- or multi-  
623 modal. Selecting the low between two modes is often straight-forward, but the thresh-  
624 old should be chosen conservatively such that all iron-oxides in the sample are selected.  
625 As de Groot et al. (2018) already noted, selecting the proper attenuation threshold para-

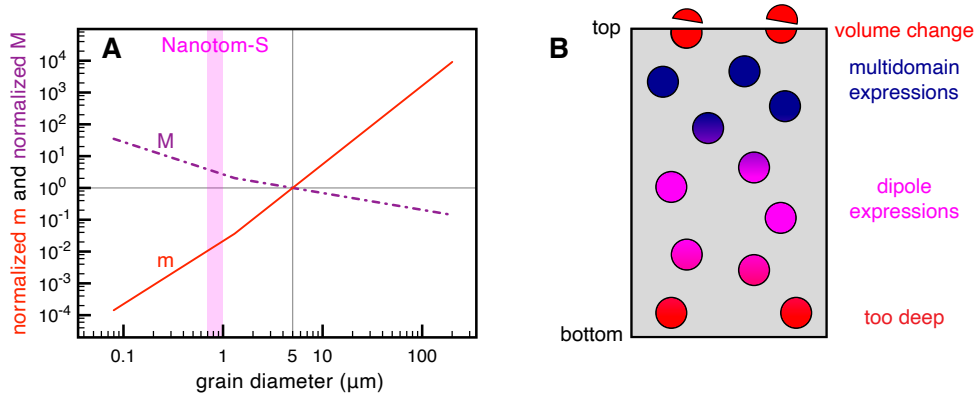


**Figure 5.** The spatial characterization of magnetic sources in a sample. The magnetization (M, in purple) and magnetic moment (m, in red) of spherical grains arising from a thermoremanent magnetic state vary as function of their diameter (A). The data are normalized to the values for a 5  $\mu\text{m}$  grain. The detection limit of the Nanotom-S microCT is in pink. Figure adapted from Fig. 7.10 in Tauxe (2010), based on data presented in Dunlop and Özdemir (1997). How well MMT can determine the magnetization of the grains (represented by the circles) depends on their depths in the sample (B). The grains at the surface are cut during sample preparation and therefore lose their natural magnetization (top grains, in red); the magnetic expression of shallow grains may represent a complex ‘multidomain’ magnetic configuration (in blue); the magnetic expression of somewhat deeper grains represent their far-field, dipolar, magnetic moment (in pink); and the magnetic anomalies arising from grains that are too deep in the sample (in red) may be too weak to be properly inverted into the magnetization of the grain.

626 doxically was easier for the volcanic sample with less distinct density differences between  
627 the grains, than for our synthetic sample with large differences in density between the  
628 matrix and the magnetite grains. The smaller differences in density most probably sup-  
629 press adverse beam hardening effects and therefore boundaries between grains are bet-  
630 ter defined in the scans.

631 The resolution of the microCT used here and in de Groot et al. (2018), the Nanotom-  
632 S at TU Delft, is  $\sim 0.7 \mu\text{m}$ , so it inherently misses grains that are below  $\sim 1 \mu\text{m}$  (Fig.  
633 5A). The grains in the synthetic sample that we used were sieved to be larger than  $3 \mu\text{m}$ ,  
634 but in natural samples many grains with sizes between the superparamagnetic thresh-  
635 old of 30-50 nm (Dunlop & Özdemir, 1997) and the resolution limit of the Nanotom-S  
636 may be present. Such smaller grains, however, have not been observed on a large scale  
637 in the Scanning Electron Microscopy, Microprobe, and Magnetic Force Microscopy ex-  
638 periments on sister specimens of our HW03 sample (ter Maat et al., 2018), while these  
639 techniques do have the necessary resolution to detect much smaller grains than the mi-  
640 croCT used in this study. Furthermore, it is important to keep in mind that relatively  
641 small grains that may be missed by the microCT analysis have relatively little contri-  
642 bution to the total magnetic signal of volcanic samples. Although the TRM of a grain  
643 with a diameter of 100 nm is 28 times higher than the TRM of a grain with a diame-  
644 ter of  $5 \mu\text{m}$  (Fig. 5A); when the volumes of these grains are taken into account and their  
645 magnetic moments ( $m$ ) are considered, the magnetic moment of the  $5 \mu\text{m}$  grain becomes  
646  $4.5 \times 10^3$  times larger than the magnetic moment of the 100 nm grain. This implies that  
647  $4.5 \times 10^3$  grains of 100 nm have to be uniformly magnetized to produce the same mag-  
648 netic moment as one grain with a diameter of  $5 \mu\text{m}$ . In a natural sample where grains  
649 are not uniformly magnetized, however, it is more likely that  $10^5$  to  $10^6$  100 nm grains  
650 are necessary to produce the same net moment as one  $5 \mu\text{m}$  grain. This illustrates that  
651 the larger grains can very well be dominant in the overall magnetic signal of a sample.

652 Current advancements in microCT scanners allow for resolutions down to  $\sim 100$   
653 nm, this is very close to the superparamagnetic threshold of 30-50 nm for magnetite grains  
654 (Dunlop & Özdemir, 1997). This implies that it is already technically possible to detect  
655 iron-oxides down to volumes where their contributions to the total magnetization of the  
656 sample becomes de facto negligible compared to the contributions of larger grains. Hence  
657 it is already possible to detect all (relevant) iron-oxides in natural samples, although the  
658 field of view of scans with such high resolution is often relatively narrow and many scans

659 should be combined to characterize the necessary amount of iron-oxide grains for paleo-  
660 omagnetic interpretations.

### 661 **5.1.2 Variation in iron-oxides**

662 Not all iron-oxide grains do have remanent magnetizations at room temperature.  
663 The Ti-rich end-members of the titanomagnetite and titanohematite solid solutions (ülvospinel  
664 and ilmenite, respectively), for example, have Curie temperatures  $< -100^{\circ}\text{C}$  (Readman  
665 & O'Reilly, 1972). To make it even more complex, Scanning Electron Microscope (SEM)  
666 studies show that large iron-oxide grains in natural lavas often exhibit several regions  
667 of different composition or show exsolution lamellae (e.g.: de Groot, Dekkers, et al., 2014;  
668 Greve et al., 2017; Monster et al., 2018). This is certainly the case for our volcanic sam-  
669 ple, HW03 (de Groot et al., 2013), as illustrated with a sister specimen taken from the  
670 same paleomagnetic drill core that was used to prepare the sample in this study from  
671 by ter Maat et al. (2018). In this study it was confirmed that zones that are identified  
672 as ilmenite by Scanning Electron Microscope, Electron Back-Scatter Diffraction, and Mi-  
673 croprobe analyses are indeed non-magnetic at room temperature by Magnetic Force Mi-  
674 croscopy. Currently it is impossible to spatially discriminate between magnetic and non-  
675 magnetic zones inside grains with the microCT techniques we used. Therefore many of  
676 the grains in our natural sample will have non-magnetic zones; i.e. their 'magnetic grain  
677 size' is often smaller than the physical grain size detected by microCT analysis. This im-  
678 plies that the volumes used to estimate the magnetizations of individual grains are of-  
679 ten larger than the regions that actually carry a magnetization in the iron-oxide grains,  
680 leading to estimates of the magnetizations that are too low. This effect, however, does  
681 not impact the magnetic moments of the grains, since they are insensitive to their vol-  
682 umes.

683 The grains in both our synthetic and volcanic sample are mostly spherical in shape.  
684 From SEM studies it is known that in many lava samples that produce accurate paleo-  
685 ointensities dendritic iron-oxide grains are the dominant magnetic carrier (e.g.: Cromwell  
686 et al., 2015; ter Maat et al., 2018). It is postulated that individual branches of dendritic  
687 grains act as small, individual, magnetic grains, with a favorable magnetic behavior com-  
688 pared to larger spherical grains. Because of resolution limits and noise effects such as  
689 beam hardening these dendritic grains are more difficult to characterize by microCT anal-  
690 yses. Moreover, it is currently unclear how the magnetic behavior of dendritic grains should

691 be modeled in an MMT inversion. Dendritic grains therefore currently pose a challenge  
 692 to be properly resolved in MMT studies.

### 693 *5.1.3 Spatial limitations as function of depth*

694 The MMT technique determines magnetizations of all grains in the sample from  
 695 a magnetic surface scan of such a sample. The expression of a grain's magnetization on  
 696 the sample's surface decays as function of depth in the sample to the power of three. This  
 697 implies that the depth of a grain dictates how well MMT can resolve its magnetization  
 698 (Fig. 5B). Grains on the surface of a sample are cut during sample processing and pol-  
 699 ishing. Therefore their volume changed and their natural magnetization is lost. For grains  
 700 close to the surface but not physically altered during sample processing we often observe  
 701 complex magnetic anomalies on the surface of the sample (e.g. Fig. 3C). We explain these  
 702 as expressions of multidomain configurations in the grains. These complex anomalies in  
 703 the magnetic surface scan violate our assumption to assign a dipolar magnetization to  
 704 each individual grain, hence they are often left in the residuals after the inversion. It is  
 705 debatable how well the dipole estimate actually represents the magnetization of grains  
 706 in this zone of 'multidomain expressions' (Fig. 5B). For deeper grains the magnetic ex-  
 707 pression on the surface represent more a 'far-field' magnetization - i.e. a dipolar mag-  
 708 netic configuration. For this zone of 'dipole expressions' MMT is able to reliably deter-  
 709 mine the dipole moment of individual grains. For even deeper grains the magnetic ex-  
 710 pression on the surface of the sample becomes so weak that it becomes impossible to re-  
 711 liably invert for their magnetizations.

712 The specific depths of the different zones depend mostly on the sample-sensor dis-  
 713 tance and the noise-level/sensitivity of the magnetic scan used. This is best illustrated  
 714 by comparing our MTJ experiment (with a scan height of 33.56  $\mu\text{m}$ ) to the QDM study  
 715 (with a scan height of 6  $\mu\text{m}$ ) on the same synthetic sample. In the MTJ experiment there  
 716 are hardly complex magnetic anomalies left in the residuals (Fig. 2C), while they are ev-  
 717 ident in the residuals of the QDM scan (Fig. 3C). The larger scan height of the MTJ  
 718 leads to detecting more of a far-field magnetic expression of the magnetization of the shal-  
 719 lower grains, and therefore a better approximation of their dipole fields. The zone of 'mul-  
 720 tidomain expressions' (Fig. 5B) is thus much smaller (if not absent) in the MTJ exper-  
 721 iment. The inversion of the MTJ experiment, however, assigns more unrealistically large  
 722 magnetizations to mostly deeper grains in the sample (compare Fig. 2D and Fig. 3D).

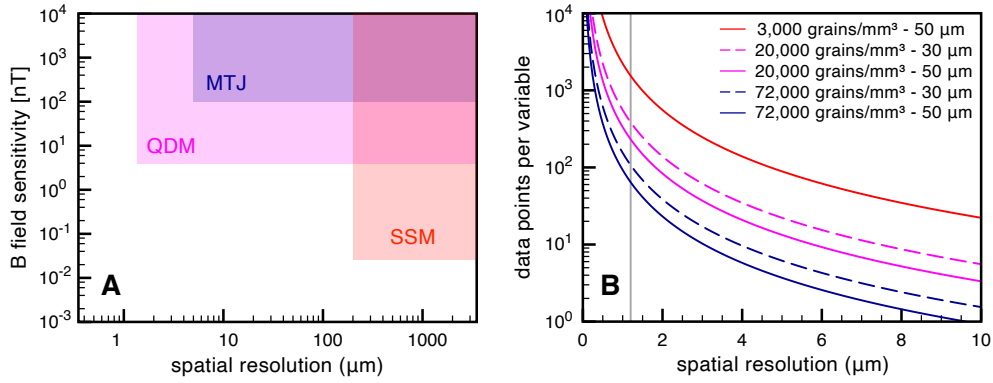


**Figure 6.** The resolution of the magnetic surface scan. Three potential scanning magnetometry techniques for MMT have different specifications for spatial resolution and B field sensitivity (A) (with data from: Lima et al., 2014; Glenn et al., 2017; Oda et al., 2016; Fu et al., 2020). The theoretically available number of data points per variable that is to be solved by the MMT inversion is governed by the concentration of grains in the sample, the thickness of the sample and the spatial resolution (i.e. step size) of the magnetic scan (B). The theoretically available number of data points per variable are given for the synthetic sample (3,000 grains/ $\text{mm}^3$  - 50  $\mu\text{m}$ ), and different grain concentrations and sample thicknesses for volcanic samples. The typical spatial resolution of the QDM (1.2  $\mu\text{m}$ ) is indicated by the gray line.

723 These are explained by the large scan height of the MTJ: the total source-sensor distance  
 724 can be  $> 80 \mu\text{m}$ . This implies that the anomalies arising from deeper grains as measured  
 725 by the MTJ sensor are very weak. This makes it difficult for the inversion to reliably de-  
 726 termine their dipole magnetization; a weak magnetic anomaly often ‘disappears’ in the  
 727 noise level of the magnetic scan - generally leading to overestimates of the dipole mag-  
 728 netizations of these deeper grains. The zone of ‘dipolar expressions’ allowing for success-  
 729 ful dipole inversions in the MTJ data is thus closer to the surface than for the QDM scan.

## 730 5.2 Scanning magnetometry

731 We demonstrated that the MMT technique can be used with different magnetic sur-  
 732 face scanning techniques. The potential of each of these techniques for MMT is governed  
 733 by their spatial resolution and sensitivity (Fig. 6A). The necessary spatial resolution of  
 734 the magnetic scan is dictated by the concentration of magnetic grains in the sample and  
 735 the sample thickness (Fig. 6B). Considering that grains are randomly distributed in a

736 sample and grains can be in very close proximity to each other, and may also be located  
737 above and below each other, not all grains are very well separable in a magnetic surface  
738 scan. A higher concentration of grains in a sample obviously leads to more magnetically  
739 obscured grains. The MMT inversion performs best if the system is vastly over-determined  
740 - i.e. when there are many data points in the magnetic surface scan per variable to solve.  
741 To provide a dipole magnetization for a grain the three orthogonal axes of the magne-  
742 tization have to be solved for; the amount of variables in the system is therefore three  
743 times the amount of grains present in the sample.

744 There are 128 individual magnetic grains in our synthetic sample; this implies a  
745 concentration of  $\sim 3,000$  grains/mm<sup>3</sup>. The concentration in the natural volcanic sam-  
746 ple is highly variable throughout the sample. For the four regions that we analyzed the  
747 concentration is  $\sim 20,000$  grains/mm<sup>3</sup> (Table 1). When the entire microCT scan of the  
748 sample is considered, the average concentration is much higher:  $\sim 72,000$  grains/mm<sup>3</sup>  
749 (de Groot et al., 2018). Given the thickness of the samples (Table 1) we can calculate  
750 the theoretical amount of data points in a magnetic surface scan per variable to solve  
751 as function of the resolution of the magnetic scan (Fig. 6B). The spatial resolution of  
752 the MTJ scan was 10  $\mu$ m, which was sufficient to determine individual magnetizations  
753 for grains in the synthetic sample (the red line in Fig. 6B). For volcanic samples, how-  
754 ever, the amount of data points per variable quickly drops to  $< 10$  for a spatial reso-  
755 lution of 10  $\mu$ m, even for a sample that is ‘only’ 30  $\mu$ m thick. The MMT inversion strug-  
756 gles to determine the magnetizations of individual grains in this case, certainly if grains  
757 are physically not well separated in the sample. The spatial resolution that can be at-  
758 tained with the QDM set-up, 1.2  $\mu$ m (Glenn et al., 2017), yields  $> 70$  data points per  
759 variable, also for the volcanic sample configurations (Fig. 6B). This provides the nec-  
760 essary amount of data points for a well-posed MMT inversion. To summarize, while the  
761 MTJ technique is well-suited for MMT inversions for samples with relatively low con-  
762 centrations of magnetic grains, the QDM set-up currently is the best magnetic scanning  
763 technique for MMT analyses on natural volcanic samples.

### 764 **5.3 The rock-magnetic potential of MMT**

765 The study of rock-magnetic processes governing the acquisition and storage of com-  
766 plex magnetizations in Earth materials has kept track with the pace of technological ad-  
767 vances in magnetic scanning techniques. In the 1980s and 1990s the resolution and sen-

768 sitivity of scanning magnetometry only allowed for characterizing magnetic domain con-  
769 figurations inside large magnetic grains. This was done by making Bitter patterns (e.g.  
770 Halgedahl, 1987, 1991), using the magneto-optical Kerr effect (e.g. Ambatiello & Sof-  
771 fel, 1996; Ambatiello et al., 1999), or with Magnetic Force Microscopy (e.g. Williams et  
772 al., 1992; Pokhil & Moskowitz, 1996, 1997; Foss et al., 1998; de Groot, Fabian, et al., 2014).  
773 These studies yielded valuable insights in the way large iron-oxides get and stay mag-  
774 netized. Simultaneously, theoretical studies modeled the magnetic behavior of large iron-  
775 oxide grains by taking a more fundamental approach to rock-magnetism (e.g. Moon &  
776 Merrill, 1984, 1985; Song Xu & Merrill, 1989, 1990). More recent technological advances  
777 took magnetic imaging down to atomic scales. Both Electron Holography (e.g. Harri-  
778 son et al., 2002; Feinberg et al., 2006; Almeida et al., 2014; Almeida, Muxworthy, Kovács,  
779 Williams, Nagy, et al., 2016; Almeida, Muxworthy, Kovács, Williams, Brown, & Dunin-  
780 Borkowski, 2016) and X-ray Photoemission Electron Microscopy (e.g. Bryson et al., 2014;  
781 Nichols et al., 2016) allow for a magnetic characterization at nm-scale and yielded in-  
782 dispensable information on the internal magnetic behavior of naturally occurring min-  
783 erals. The development of MERRILL, an open source software package for three-dimensional  
784 micromagnetics (Conbhúí et al., 2018), enabled computationally assessing the magnetic  
785 behavior of relatively small ( $< 1 \mu\text{m}$ ) grains.

786 Despite the aforementioned progress the interpretations of magnetic surface scans  
787 was still often two-dimensional; relied on an upward continuation (Blakely, 1996; Lima  
788 & Weiss, 2009; Lima et al., 2014; Lima & Weiss, 2016; Fu et al., 2020); or needed other  
789 additional assumptions. By adding a spatial characterization of the magnetic sources in  
790 the sample, the MMT technique overcame this classical inversion problem (Kellogg, 1929)  
791 and now allows for characterizing the three-dimensional magnetic moment of individ-  
792 ual grains inside a sample. It is important to emphasize that the magnetic surface scan-  
793 ning techniques used in this study are non-destructive. MMT experiments can thus be  
794 repeated after laboratory treatments on the sample. This opens up entirely new venues  
795 for rock-magnetic research: now the magnetic state of individual grains can be assessed  
796 as function of magnetic treatment, size, shape, and possibly chemistry. This will lead  
797 to valuable insights in which grains are capable of recording the Earth's magnetic field  
798 and retaining that information over geologic time, and which grains should be avoided.

799 Building on a recent proof of uniqueness for microCT assisted potential field in-  
800 versions using spherical harmonics (Fabian & de Groot, 2019), it was shown that MMT

801 also allows to invert for higher order descriptions of the magnetic state of individual grains  
802 in a sample (Cortés-Ortuño et al., 2021). Beyond the dipolar magnetic moments, the quadrupole  
803 and octupole descriptions provide insight in the complexity of the magnetic stray fields  
804 of individual grains in a sample. While the non-uniqueness of the classical potential in-  
805 version problem (Kellogg, 1929) once again implies that it is impossible to directly in-  
806 vert for the internal domain structure of individual grains without further a priori con-  
807 straints, the higher-order descriptions of their stray field can help to assess the complex-  
808 ity of the internal magnetic structure of individual grains (Cortés-Ortuño et al., 2021).  
809 This may eventually bridge the gap between magnetic imaging techniques and compu-  
810 tational micromagnetic models, and enable the development of a comprehensive, fun-  
811 damental theory for the processes governing the acquisition and preservation of magnetic  
812 signals in multi-domain grains in the future.

#### 813 **5.4 The paleomagnetic potential of MMT**

814 When we are able to identify which grains are good paleomagnetic recorders, and  
815 which are the bad ones, it becomes possible to use MMT to its full potential and obtain  
816 paleomagnetic information from only the most reliable recorders in a sample. The ac-  
817 quisition of magnetizations in iron-oxides is a statistical process. For small, single-domain  
818 grains the moments of  $10^6$  to  $10^8$  grains must be considered before the direction and in-  
819 tensity of the resulting magnetic moment represent the direction and intensity of the am-  
820 bient magnetic field at the time of cooling (Berndt et al., 2016). When measuring bulk  
821 samples this happens implicitly, standard size paleomagnetic samples contain in the or-  
822 der of  $10^8$  to  $10^9$  magnetic grains, and the bulk signal is a statistical ensemble of the mag-  
823 netizations of all these grains together.

824 Berndt et al. (2016) used Néel’s theory on thermoremanent magnetizations in single-  
825 domain ferromagnetic minerals (Néel, 1949, 1955) for their estimations. Single domain  
826 grains cannot optimize their internal domain structure, as larger multi-domain grains  
827 can. During acquisition of their magnetization multi-domain grains statistically end up  
828 in a local energy minimum, with an associated domain configuration. But these grains  
829 have many possible local energy minima and domain configurations. Depending on the  
830 nature and strength of the imparting field the local energy minimum more or less rep-  
831 represents the imparting magnetic field. In our experiments to determine a magnetic direc-  
832 tion from subsets of grains in our synthetic sample, we strongly magnetized our sample

833 by giving it an IRM at 1 T. We showed that it is possible to obtain an average direction  
834 that is only  $0.2^\circ$  to  $12.9^\circ$  off of the direction of the applied field (Figs. 2F and 3F), af-  
835 ter selecting grains with low remanence ratios from 128 grains in the sample. The IRM  
836 acquisition is generally reported to be 100 times more efficient than TRM acquisition  
837 (e.g. Fuller et al., 1988). This could imply that for TRMs in multi-domain grains  $10^4$   
838 to  $10^5$  grains may already provide meaningful paleomagnetic information derived from  
839 subsets of individual grains in a sample, although this is currently highly speculative.

840 To assess whether it is both empirically and computationally possible to use MMT  
841 to determine naturally occurring paleodirections and paleointensities we assume that we  
842 need to sum the magnetic moments of  $10^5$  grains from a sample. With a concentration  
843 of 72,000 grains/ $\text{mm}^3$  in a volcanic sample (de Groot et al., 2018) and a sample thick-  
844 ness of 50  $\mu\text{m}$ , there are 3,600 grains per  $\text{mm}^2$  of such a sample. This implies that 28  
845  $\text{mm}^2$  of sample would be sufficient. This is challenging, but not impossible for our cur-  
846 rent magnetic scanning and microCT analyses. The current inversion routine, however,  
847 is not optimized for computational efficiency, yet. Hence, we are currently limited to in-  
848 vert only small parts of a sample (e.g. Fig. 4), with low numbers of grains ( $<100$ ). More-  
849 over, the inversions are performed on a modest quad-core desktop computer. By opti-  
850 mizing the code for a multi-core machine and using a computational cluster it is possi-  
851 ble to gain one to two orders of magnitude in speed. The computational demands can  
852 be further decreased by using the full potential of the recent proof of uniqueness for mi-  
853 croCT assisted potential field inversions using spherical harmonics (Fabian & de Groot,  
854 2019). A new inversion algorithm based on this concept promises to reduce the quadratic  
855 dependence of calculation time on the number of grains in the current inversion algo-  
856 rithm to an almost linear dependence, which will greatly reduce computational time. To  
857 summarize, ongoing developments allow for an increase of at least three orders of mag-  
858 nitude in computational speed. This makes it possible to invert for  $> 10^5$  grains and  
859 enables determining magnetic directions and intensities from individual grains in a sam-  
860 ple.

861 A unique feature of MMT is the possibility to derive paleomagnetic information  
862 from subsets of grains in the sample. Here we used a rather crude selection criterion for  
863 the grains based on their remanence ratios. It is important to emphasize once more that  
864 the magnetic surface scanning techniques used in this study are non-destructive. This  
865 implies that it is possible to mimic traditional paleomagnetic experiments such as step-

866 wise demagnetization, or paleointensity experiments, while interpreting the magnetiza-  
867 tion of individual grains. Also, these traditional paleomagnetic experiments may pro-  
868 vide additional information on how to discriminate between grains with good and bad  
869 magnetic recording properties, further testifying to the paleomagnetic potential of MMT.

## 870 **6 Conclusions and Outlook**

871 We showed that MMT is capable of determining magnetic moments of individual  
872 grains in both synthetic and natural samples using different magnetic scanning techniques.  
873 Thereby MMT is established as a paleomagnetic and rock-magnetic technique and it opens  
874 up entirely new venues of paleomagnetic and rock-magnetic research. Nevertheless, two  
875 significant challenges remain before MMT can be used to its full potential. First, the res-  
876 olution of the microCT scan must be increased to detect all grains of interest, potentially  
877 down to the superparamagnetic threshold of  $\sim 50$  nm. Second, the computational power  
878 should become sufficient to solve for the large amounts of grains necessary for a proper  
879 statistical analyses of the magnetic moments obtained for individual grains. When these  
880 two issues are resolved, MMT's unique ability to determine the magnetization of indi-  
881 vidual grains in a nondestructive way will enable a systematic analysis of how naturally  
882 occurring iron-oxides record and retain information on the past state of the Earth's mag-  
883 netic field. These insights in which materials are reliable recorders of the ambient mag-  
884 netic field and which should be avoided are vital for the paleomagnetic community, and  
885 adjacent communities using paleomagnetic data such as tectonic studies, studies of the  
886 deep Earth, and (magneto-)stratigraphy.

887 By selecting only the contributions of known magnetically well-behaved grains in  
888 a sample MMT enables obtaining reliable paleomagnetic information from even the most  
889 complex, crucial, or valuable paleomagnetic recorders. This includes lavas that form an  
890 indispensable archive of geomagnetic field variations. Fully unlocking this archive is vi-  
891 tal for our understanding of the short-term variability of the Earth's magnetic field. The  
892 potential of MMT, however, is not limited to lavas; paleomagnetic information from even  
893 more unique materials can also be retrieved. This includes e.g. the oldest rocks on Earth  
894 to shed light on the origin and evolution of the Earth's core; meteorites to unravel the  
895 conditions during the formation of our Solar system; and maybe even lunar samples to  
896 elucidate its origin and evolution.

## 897 Acknowledgments

898 The data presented in this manuscript are available in the PANGAEA.de repository, DOI:  
 899 10.1594/PANGAEA.919360. This project has received funding from the European Re-  
 900 search Council (ERC) under the European Union’s Horizon 2020 research and innova-  
 901 tion programme (Grant agreement No. 851460 ‘MIMATOM’ to LVdG). LVdG acknowl-  
 902 edges funding from the Dutch Science Foundation (NWO) grant ALWOP.641. Valera  
 903 Shcherbakov and an anonymous reviewer are gratefully acknowledged for their thorough  
 904 reviews that helped to improve this manuscript.

905 Author contributions: LVdG designed the studies and wrote the manuscript together  
 906 with KF; ABé did the QDM study on a volcanic sample; ABé and MEK did the QDM  
 907 study on the synthetic sample; DCO and TvL contributed to the inverse data process-  
 908 ing and computational workflow; RFF did the QDM measurements; CMLJ did the MTJ  
 909 study with the help of RJH; ABa did the MicroCT analyses. The authors declare no com-  
 910 peting interests.

## 911 References

- 912 Almeida, T. P., Kasama, T., Muxworthy, A. R., Williams, W., Nagy, L., Hansen,  
 913 T. W., ... Dunin-Borkowski, R. E. (2014). Visualized effect of oxidation on  
 914 magnetic recording fidelity in pseudo-single-domain magnetite particles. *Nature*  
 915 *Communications*, 5(1), 5154. doi: 10.1038/ncomms6154
- 916 Almeida, T. P., Muxworthy, A. R., Kovács, A., Williams, W., Brown, P. D., &  
 917 Dunin-Borkowski, R. E. (2016). Direct visualization of the thermomagnetic  
 918 behavior of pseudo-single-domain magnetite particles. *Science Advances*, 2(4),  
 919 e1501801. doi: 10.1126/sciadv.1501801
- 920 Almeida, T. P., Muxworthy, A. R., Kovács, A., Williams, W., Nagy, L., Conbhuí, P.,  
 921 ... Dunin-Borkowski, R. E. (2016). Direct observation of the thermal demag-  
 922 netization of magnetic vortex structures in nonideal magnetite recorders. *Geo-*  
 923 *physical Research Letters*, 43(16), 8426–8434. doi: 10.1002/2016GL070074
- 924 Ambatiello, A., Fabian, K., & Hoffmann, V. (1999). Magnetic domain structure  
 925 of multidomain magnetite as a function of temperature: Observation by Kerr  
 926 microscopy. *Physics of the Earth and Planetary Interiors*, 112(1-2), 55–80.  
 927 doi: 10.1016/S0031-9201(98)00177-0
- 928 Ambatiello, A., & Soffel, H. C. (1996). Kerr microscopy of small synthetic Ti-rich ti-

- 929        titanomagnetite grains. *Geophysical Research Letters*, *23*(20), 2807–2810. doi:  
930        10.1029/96GL00447
- 931        Berndt, T., Muxworthy, A. R., & Fabian, K.        (2016).        Does size matter? Sta-  
932        tistical limits of paleomagnetic field reconstruction from small rock speci-  
933        mens. *Journal of Geophysical Research: Solid Earth*, *121*(1), 15–26. doi:  
934        10.1002/2015JB012441
- 935        Blakely, R. J. (1996). *Potential theory in gravity and magnetic applications*. Cam-  
936        bridge University Press.
- 937        Bowles, J. A., & Jackson, M. J.        (2016).        Effects of titanomagnetite reorder-  
938        ing processes on thermal demagnetization and paleointensity experi-  
939        ments. *Geochemistry, Geophysics, Geosystems*, *17*(12), 4848–4858. doi:  
940        10.1002/2016GC006607
- 941        Bowles, J. A., Jackson, M. J., Berquó, T. S., Sølheid, P. A., & Gee, J. S.        (2013).  
942        Inferred time- and temperature-dependent cation ordering in natural titano-  
943        magnetites. *Nature Communications*, *4*(1), 1916. doi: 10.1038/ncomms2938
- 944        Bryson, J. F., Herrero-Albillos, J., Kronast, F., Ghidini, M., Redfern, S. A., Van der  
945        Laan, G., & Harrison, R. J. (2014). Nanopaleomagnetism of meteoritic Fe-Ni  
946        studied using X-ray photoemission electron microscopy. *Earth and Planetary  
947        Science Letters*, *396*, 125–133. doi: 10.1016/j.epsl.2014.04.016
- 948        Coe, R. S. (1967). Paleo-intensities of the Earth’s magnetic field determined from  
949        Tertiary and Quaternary rocks. *Journal of Geophysical Research*, *72*(12),  
950        3247–3262. doi: 10.1029/JZ072i012p03247
- 951        Coe, R. S., Jarboe, N. A., LeGoff, M., & Petersen, N. (2014). Demise of the rapid-  
952        field-change hypothesis at Steens Mountain: The crucial role of continuous  
953        thermal demagnetization. *Earth and Planetary Science Letters*, *400*, 302–312.  
954        doi: 10.1016/j.epsl.2014.05.036
- 955        Conbhuí, P., Williams, W., Fabian, K., Ridley, P., Nagy, L., & Muxworthy, A. R.  
956        (2018).        Merrill: Micromagnetic earth related robust interpreted language  
957        laboratory. *Geochemistry, Geophysics, Geosystems*, *19*(4), 1080–1106. doi:  
958        10.1002/2017GC007279
- 959        Cortés-Ortuño, D. I., Fabian, K., & de Groot, L. V. (2021). *Single particle multipole  
960        expansions from micromagnetic tomography*. doi: arXiv:2101.07010
- 961        Cromwell, G., Tauxe, L., Staudigel, H., & Ron, H. (2015). Paleointensity estimates

- 962 from historic and modern Hawaiian lava flows using glassy basalt as a primary  
963 source material. *Physics of the Earth and Planetary Interiors*, 241, 44–56. doi:  
964 10.1016/j.pepi.2014.12.007
- 965 de Groot, L. V., Biggin, A. J., Dekkers, M. J., Langereis, C. G., & Herrero-Bervera,  
966 E. (2013). Rapid regional perturbations to the recent global geomagnetic decay  
967 revealed by a new Hawaiian record. *Nature Communications*, 4(1), 2727. doi:  
968 10.1038/ncomms3727
- 969 de Groot, L. V., Dekkers, M. J., Visscher, M., & ter Maat, G. W. (2014). Mag-  
970 netic properties and paleointensities as function of depth in a Hawaiian  
971 lava flow. *Geochemistry, Geophysics, Geosystems*, 15(4), 1096–1112. doi:  
972 10.1002/2013GC005094
- 973 de Groot, L. V., Fabian, K., Bakelaar, I. A., & Dekkers, M. J. (2014). Magnetic  
974 force microscopy reveals meta-stable magnetic domain states that prevent re-  
975 liable absolute palaeointensity experiments. *Nature Communications*, 5(1),  
976 4548. doi: 10.1038/ncomms5548
- 977 de Groot, L. V., Fabian, K., Béguin, A., Reith, P., Barnhoorn, A., & Hilgenkamp,  
978 H. (2018). Determining Individual Particle Magnetizations in Assem-  
979 blages of Micrograins. *Geophysical Research Letters*, 45(7), 2995–3000. doi:  
980 10.1002/2017GL076634
- 981 Dunlop, D. J. (2011). Physical basis of the Thellier-Thellier and related paleointen-  
982 sity methods. *Physics of the Earth and Planetary Interiors*, 187(3-4), 118–138.  
983 doi: 10.1016/j.pepi.2011.03.006
- 984 Dunlop, D. J., & Özdemir, O. (1997). *Rock magnetism: Fundamentals and frontiers*.  
985 Cambridge University Press. doi: 10.1017/CBO9780511612794
- 986 Egli, R., & Heller, F. (2000). High-resolution imaging using a high-Tc super-  
987 conducting quantum interference device (SQUID) magnetometer. *Jour-  
988 nal of Geophysical Research: Solid Earth*, 105(B11), 25709–25727. doi:  
989 10.1029/2000jb900192
- 990 Fabian, K. (2000). Acquisition of thermoremanent magnetization in weak magnetic  
991 fields. *Geophysical Journal International*, 142(2), 478–486. doi: 10.1046/j.1365-  
992 -246x.2000.00167.x
- 993 Fabian, K. (2001). A theoretical treatment of paleointensity determination  
994 experiments on rocks containing pseudo-single or multi domain magnetic

- 995 particles. *Earth and Planetary Science Letters*, 188(1-2), 45-58. doi:  
996 10.1016/S0012-821X(01)00313-2
- 997 Fabian, K. (2009). Thermochemical remanence acquisition in single-domain  
998 particle ensembles: A case for possible overestimation of the geomag-  
999 netic paleointensity. *Geochemistry, Geophysics, Geosystems*, 10(6). doi:  
1000 10.1029/2009GC002420
- 1001 Fabian, K., & de Groot, L. V. (2019). A uniqueness theorem for tomography-  
1002 assisted potential-field inversion. *Geophysical Journal International*, 216(2),  
1003 760–766. doi: 10.1093/gji/ggy455
- 1004 Farchi, E., Ebert, Y., Farfurnik, D., Haim, G., Shaar, R., & Bar-Gill, N. (2017).  
1005 Quantitative Vectorial Magnetic Imaging of Multi-Domain Rock Forming Min-  
1006 erals Using Nitrogen-Vacancy Centers in Diamond. *SPIN*, 07(03), 1740015.  
1007 doi: 10.1142/S201032471740015X
- 1008 Feinberg, J. M., Harrison, R. J., Kasama, T., Dunin-Borkowski, R. E., Scott, G. R.,  
1009 & Renne, P. R. (2006). Effects of internal mineral structures on the magnetic  
1010 remanence of silicate-hosted titanomagnetite inclusions: An electron hologra-  
1011 phy study. *Journal of Geophysical Research: Solid Earth*, 111(12), 1–11. doi:  
1012 10.1029/2006JB004498
- 1013 Fong, L. E., Holzer, J. R., McBride, K. K., Lima, E. A., Baudenbacher, F., & Rad-  
1014 parvar, M. (2005). High-resolution room-temperature sample scanning super-  
1015 conducting quantum interference device microscope configurable for geological  
1016 and biomagnetic applications. *Review of Scientific Instruments*, 76(5). doi:  
1017 10.1063/1.1884025
- 1018 Foss, S., Moskowitz, B. M., Proksch, R., & Dahlberg, E. D. (1998). Domain wall  
1019 structures in single-crystal magnetite investigated by magnetic force mi-  
1020 croscopy. *Journal of Geophysical Research: Solid Earth*, 103(B12), 30551–  
1021 30560. doi: 10.1029/98jb00152
- 1022 Fu, R. R., Lima, E. A., Volk, M. W., & Trubko, R. (2020). High-Sensitivity Moment  
1023 Magnetometry With the Quantum Diamond Microscope. *Geochemistry, Geo-  
1024 physics, Geosystems*, 21(8), 1–17. doi: 10.1029/2020GC009147
- 1025 Fuller, M., Cisowski, S., Hart, M., Haston, R., Schmidtke, E., & Jarrard, R. (1988).  
1026 NRM: IRM(S) demagnetization plots; An aid to the interpretation of natural  
1027 remanent magnetization. *Geophysical Research Letters*, 15(5), 518–521. doi:

- 1028 10.1029/GL015i005p00518
- 1029 Glenn, D. R., Fu, R. R., Kehayias, P., Le Sage, D., Lima, E. A., Weiss, B. P., &  
 1030 Walsworth, R. L. (2017). Micrometer-scale magnetic imaging of geological  
 1031 samples using a quantum diamond microscope. *Geochemistry, Geophysics,*  
 1032 *Geosystems*, 18(8), 3254–3267. doi: 10.1002/2017GC006946
- 1033 Greve, A., Hill, M. J., Turner, G. M., & Nilsson, A. (2017). The geomagnetic  
 1034 field intensity in New Zealand: palaeointensities from Holocene lava flows of  
 1035 the Tongariro Volcanic Centre. *Geophysical Journal International*, 211(2),  
 1036 814–830. doi: 10.1093/gji/ggx327
- 1037 Halgedahl, S. L. (1987). Domain pattern observations in rock magnetism: progress  
 1038 and problems. *Physics of the Earth and Planetary Interiors*, 46(1-3), 127–163.  
 1039 doi: 10.1016/0031-9201(87)90178-6
- 1040 Halgedahl, S. L. (1991). Magnetic domain patterns observed on synthetic Ti-rich  
 1041 titanomagnetite as a function of temperature and in states of thermoremanent  
 1042 magnetization. *Journal of Geophysical Research*, 96(B3), 3943–3972. doi:  
 1043 10.1029/90JB00014
- 1044 Harrison, R. J., Dunin-Borkowski, R. E., & Putnis, A. (2002). Direct imaging  
 1045 of nanoscale magnetic interactions in minerals. *Proceedings of the National*  
 1046 *Academy of Sciences of the United States of America*, 99(26), 16556–16561.  
 1047 doi: 10.1073/pnas.262514499
- 1048 Heidig, T., Zeiser, T., & Freund, H. (2017). Influence of resolution of rasterized  
 1049 geometries on porosity and specific surface area exemplified for model geome-  
 1050 tries of porous media. *Transport in Porous Media*, 120(1), 207–225. doi:  
 1051 10.1007/s11242-017-0916-y
- 1052 Jussiani, E. I., & Appoloni, C. R. (2015). Effective atomic number and density de-  
 1053 termination of rocks by x-ray microtomography. *Micron*, 70, 1-6. doi: [https://](https://doi.org/10.1016/j.micron.2014.11.005)  
 1054 [doi.org/10.1016/j.micron.2014.11.005](https://doi.org/10.1016/j.micron.2014.11.005)
- 1055 Kellogg, O. D. (1929). *Foundations of potential theory*. Springer Berlin Heidelberg.  
 1056 doi: 10.1007/978-3-642-90850-7
- 1057 Kirtley, J. R., & Wikswo, J. P. (1999). Scanning squid microscopy. *Annual Review*  
 1058 *of Materials Science*, 29(1), 117–148. doi: 10.1146/annurev.matsci.29.1.117
- 1059 Levine, E. V., Turner, M. J., Kehayias, P., Hart, C. A., Langellier, N., Trubko,  
 1060 R., . . . Walsworth, R. L. (2019). Principles and techniques of the quan-

- 1061 tum diamond microscope. *Nanophotonics*, 8(11), 1945–1973. doi:  
 1062 10.1515/nanoph-2019-0209
- 1063 Lima, E. A., Bruno, A. C., Carvalho, H. R., & Weiss, B. P. (2014). Scanning  
 1064 magnetic tunnel junction microscope for high-resolution imaging of remanent  
 1065 magnetization fields. *Measurement Science and Technology*, 25(10), 105401.  
 1066 doi: 10.1088/0957-0233/25/10/105401
- 1067 Lima, E. A., & Weiss, B. P. (2009). Obtaining vector magnetic field maps from  
 1068 single-component measurements of geological samples. *Journal of Geophysical  
 1069 Research*, 114(B6), B06102. doi: 10.1029/2008JB006006
- 1070 Lima, E. A., & Weiss, B. P. (2016). Ultra-high sensitivity moment magnetometry  
 1071 of geological samples using magnetic microscopy. *Geochemistry, Geophysics,  
 1072 Geosystems*, 17(9), 3754–3774. doi: 10.1002/2016GC006487
- 1073 Lima, E. A., Weiss, B. P., Baratchart, L., Hardin, D. P., & Saff, E. B. (2013). Fast  
 1074 inversion of magnetic field maps of unidirectional planar geological magnetiza-  
 1075 tion. *Journal of Geophysical Research: Solid Earth*, 118(6), 2723–2752. doi:  
 1076 10.1002/jgrb.50229
- 1077 Madonna, C., Almqvist, B. S., & Saenger, E. H. (2012). Digital rock physics:  
 1078 numerical prediction of pressure-dependent ultrasonic velocities using micro-  
 1079 CT imaging. *Geophysical Journal International*, 189(3), 1475–1482. doi:  
 1080 10.1111/j.1365-246X.2012.05437.x
- 1081 Monster, M. W., Langemeijer, J., Wiarda, L. R., Dekkers, M. J., Biggin, A. J.,  
 1082 Hurst, E. A., & de Groot, L. V. (2018). Full-vector geomagnetic field records  
 1083 from the East Eifel, Germany. *Physics of the Earth and Planetary Interiors*,  
 1084 274(December 2017), 148–157. doi: 10.1016/j.pepi.2017.11.009
- 1085 Moon, T. S., & Merrill, R. T. (1984). The magnetic moments of non-uniformly mag-  
 1086 netized grains. *Physics of the Earth and Planetary Interiors*, 34(3), 186–194.  
 1087 doi: 10.1016/0031-9201(84)90006-2
- 1088 Moon, T. S., & Merrill, R. T. (1985). Nucleation theory and domain states in mul-  
 1089 tidomain magnetic material. *Physics of the Earth and Planetary Interiors*,  
 1090 37(2-3), 214–222. doi: 10.1016/0031-9201(85)90053-6
- 1091 Moore, E. H. (1920). Abstract for “On the reciprocal of the general algebraic ma-  
 1092 trix”. *Bulletin of the American Mathematical Society*, 26, 394–395.
- 1093 Néel, L. (1949). Théorie du traînage magnétique des ferromagnétiques en grains fins

- 1094 avec application aux terres cuites. *Annales de Geophysique*, 5, 99–136.
- 1095 Néel, L. (1955). Some theoretical aspects of rock-magnetism. *Advances in Physics*,
- 1096 4(14), 191–243. doi: 10.1080/00018735500101204
- 1097 Nichols, C. I., Bryson, J. F., Herrero-Albillos, J., Kronast, F., Nimmo, F., &
- 1098 Harrison, R. J. (2016). Pallasite paleomagnetism: Quiescence of a
- 1099 core dynamo. *Earth and Planetary Science Letters*, 441, 103–112. doi:
- 1100 10.1016/j.epsl.2016.02.037
- 1101 Oda, H., Kawai, J., Miyamoto, M., Miyagi, I., Sato, M., Noguchi, A., ... Xuan, C.
- 1102 (2016). Scanning SQUID microscope system for geological samples: System
- 1103 integration and initial evaluation. *Earth, Planets and Space*, 68(1), 179. doi:
- 1104 10.1186/s40623-016-0549-3
- 1105 Penrose, R. (1955). A generalized inverse for matrices. *Mathematical Pro-*
- 1106 *ceedings of the Cambridge Philosophical Society*, 51(3), 406–413. doi:
- 1107 10.1017/S0305004100030401
- 1108 Pokhil, T. G., & Moskowitz, B. M. (1996). Magnetic force microscope study of
- 1109 domain wall structures in magnetite. *Journal of Applied Physics*, 79(8 PART
- 1110 2B), 6064–6066. doi: 10.1063/1.362093
- 1111 Pokhil, T. G., & Moskowitz, B. M. (1997). Magnetic domains and domain walls
- 1112 in pseudo-single-domain magnetite studied with magnetic force microscopy.
- 1113 *Journal of Geophysical Research: Solid Earth*, 102(B10), 22681–22694. doi:
- 1114 10.1029/97jb01856
- 1115 Prévot, M., Mankinen, E. A., Grommé, C. S., & Coe, R. S. (1985). How the geo-
- 1116 magnetic field vector reverses polarity. *Nature*, 316(6025), 230–234. doi: 10
- 1117 .1038/316230a0
- 1118 Readman, P. W., & O'Reilly, W. (1972). Magnetic Properties of Oxidized (Cation-
- 1119 Deficient) Titanomagnetites (Fe, Ti, □)<sub>3</sub>O<sub>4</sub>. *Journal of geomagnetism and geo-*
- 1120 *electricity*, 24(1), 69–90. doi: 10.5636/jgg.24.69
- 1121 Reith, P., Renshaw Wang, X., & Hilgenkamp, H. (2017). Analysing magnetism us-
- 1122 ing scanning squid microscopy. *Review of scientific instruments*, 88(12). doi:
- 1123 10.1063/1.5001390
- 1124 Sakellariou, A., Sawkins, T., Senden, T., & Limaye, A. (2004). X-ray tomogra-
- 1125 phy for mesoscale physics applications. *Physica A: Statistical Mechanics and*
- 1126 *its Applications*, 339(1-2), 152–158. doi: 10.1016/j.physa.2004.03.055

- 1127 Shaar, R., Ron, H., Tauxe, L., Kessel, R., & Agnon, A. (2011). Paleomagnetic field  
 1128 intensity derived from non-SD: Testing the Thellier IZZI technique on MD  
 1129 slag and a new bootstrap procedure. *Earth and Planetary Science Letters*,  
 1130 *310*(3-4), 213–224. doi: 10.1016/j.epsl.2011.08.024
- 1131 Shcherbakov, V. P., Gribov, S. K., Lhuillier, F., Aphinogenova, N. A., &  
 1132 Tsel'movich, V. A. (2019). On the Reliability of Absolute Palaeointen-  
 1133 sity Determinations on Basaltic Rocks Bearing a Thermochemical Rema-  
 1134 nence. *Journal of Geophysical Research: Solid Earth*, *124*(8), 7616–7632. doi:  
 1135 10.1029/2019JB017873
- 1136 Shcherbakova, V. V., Shcherbakov, V. P., & Heider, F. (2000). Properties of partial  
 1137 thermoremanent magnetization in pseudosingle domain and multidomain mag-  
 1138 netite grains. *Journal of Geophysical Research: Solid Earth*, *105*(B1), 767–781.  
 1139 doi: 10.1029/1999JB900235
- 1140 Song Xu, & Merrill, R. T. (1989). Microstress and microcoercivity in multidomain  
 1141 grains. *Journal of Geophysical Research*, *94*(B8), 10627–10636. doi: 10.1029/  
 1142 jb094ib08p10627
- 1143 Song Xu, & Merrill, R. T. (1990). Microcoercivity, bulk coercivity and saturation re-  
 1144 manence in multidomain materials. *Journal of Geophysical Research*, *95*(B5),  
 1145 7083–7090. doi: 10.1029/jb095ib05p07083
- 1146 Tauxe, L. (2010). *Essentials of paleomagnetism*. University of California Press.
- 1147 Tauxe, L., & Yamazaki, T. (2015). Paleointensities. In *Treatise on geophysics* (pp.  
 1148 461–509). Elsevier. doi: 10.1016/B978-0-444-53802-4.00107-X
- 1149 ter Maat, G. W., Pennock, G. M., & de Groot, L. V. (2018). Data descrip-  
 1150 tor: A chemical, crystallographic and magnetic characterisation of indi-  
 1151 vidual iron-oxide grains in Hawaiian lavas. *Scientific Data*, *5*, 1–9. doi:  
 1152 10.1038/sdata.2018.162
- 1153 Thellier, E., & Thellier, O. (1959). Sur L'intensité de champ magnétique terrestre  
 1154 dans le passé historique et géologique. *Annales de Geophysique*, *15*, 285–376.
- 1155 Valet, J. P. (2003). Time variations in geomagnetic intensity. *Reviews of Geophysics*,  
 1156 *41*(1), 1004. doi: 10.1029/2001RG000104
- 1157 Weiss, B. P., Lima, E. A., Fong, L. E., & Baudenbacher, F. J. (2007). Paleomag-  
 1158 netic analysis using SQUID microscopy. *Journal of Geophysical Research: Solid*  
 1159 *Earth*, *112*(9), B09105. doi: 10.1029/2007JB004940

1160 Williams, W., Hoffmann, V., Heider, F., Goddenhenrich, T., & Heiden, C. (1992).  
1161 Magnetic force microscopy imaging of domain walls in magnetite. *Geophysical*  
1162 *Journal International*, 111(3), 417–423. doi: 10.1111/j.1365-246X.1992.tb02100  
1163 .X